TPL2 kinase activity regulates microglial inflammatory responses and promotes neurodegeneration in tauopathy mice

Yuanyuan Wang[1,*], Tiffany Wu[1], Ming-Chi Tsai[1], Mitchell G Rezzonico[2], Alyaa M Abdel-Haleem[3], Luke Xie[4], Vineela D Gandham[4], Hai Ngu[5], Kimberly Stark[1], Caspar Glock[2], Daqi Xu[6], Oded Foreman[5], Brad A Friedman[2], Morgan Sheng[1,7], Jesse E Hanson[1,*]

[1]Department of Neuroscience, Genentech Inc.; South San Francisco, CA 94080, USA.
[2]Department of OMNI Bioinformatics, Genentech Inc.; South San Francisco, CA 94080, USA.
[3]Computational Science & Exploratory Analytics, Roche IT, Hoffmann-La Roche Limited; Mississauga, ON L5N 5M8, Canada.
[4]Department of Biomedical Imaging, Genentech Inc.; South San Francisco, CA 94080, USA.
[5]Department of Pathology, Genentech Inc.; South San Francisco, CA 94080, USA.
[6]Department of Immunology, Genentech Inc.; South San Francisco, CA 94080, USA.
[7]Stanley Center for Psychiatric Research, Broad Institute of MIT and Harvard; Cambridge, MA 02142, USA.
*Correspondence: wang.yuanyuan@gene.com, hanson.jesse@gene.com

Abstract

TPL2 (MAP3K8) is a central signaling node in the inflammatory response of peripheral immune cells. We find that TPL2 kinase activity modulates microglial cytokine release and is required for microglia-mediated neuron death *in vitro*. In acute *in vivo* neuroinflammation settings, TPL2 kinase activity regulates microglia activation states and brain cytokine levels. In a tauopathy model of chronic neurodegeneration, loss of TPL2 kinase activity reduces neuroinflammation and rescues synapse loss, brain volume loss, and behavioral deficits. Single-cell RNAseq analysis indicates protection in the tauopathy model was associated with reductions in activated microglia subpopulations as well as infiltrating peripheral immune cells. Overall, using various models, we find that TPL2 kinase activity can promote multiple harmful consequences of microglial activation in the brain including cytokine release, iNOS induction, astrocyte activation, and immune cell infiltration. Consequently, inhibiting TPL2 kinase activity could represent a potential therapeutic strategy in neurodegenerative conditions.

Introduction

Activation of microglia, the tissue resident macrophages of the brain, occurs in numerous neurodegenerative conditions including Alzheimer's disease (AD) and frontotemporal dementia (FTD), where microglia are activated in response to amyloid and tau pathology. While microglia activation may facilitate beneficial functions, such as clearance of amyloid plaques, in the early stages of AD, chronic microglia activation could contribute to disease progression via cytokine release and other harmful functions during later stages of disease (Bright et al., 2019; Hansen et al., 2018; Leng and Edison, 2021). A pathogenic role for inflammatory cytokines in neurodegeneration is supported by the increased risk for AD in people with rheumatoid arthritis (RA), psoriasis, and other inflammatory diseases, and a significantly reduced incidence of AD for those patients that received treatment with TNF blocking agents (Zhou et al., 2020). Several aspects of neuroinflammation that have been observed in neurodegeneration patient brains have been studied in preclinical models and found to have deleterious effects. This includes studies in AD and FTD models that identify harmful effects of activated astrocytes (Liddelow et al., 2017), NLRP3 inflammasome activation (Heneka et al., 2013; Ising et al., 2019), complement pathway activation (Dejanovic et al., 2018; Hong et al., 2016; Wu et al., 2019), and infiltration of T cells (Gate et al., 2020; Laurent et al., 2017; Merlini et al., 2018).

Given such diverse mediators of the detrimental effects of neuroinflammation and microglia activation, targeting a central regulator of inflammatory function represents an attractive therapeutic approach. We therefore focused on tumor progression locus 2 (TPL2), a kinase that is

expressed in both adaptive and innate immune cells in the peripheral system and plays central roles in regulating inflammatory responses. TPL2 is a mitogen-activated protein kinase kinase kinase (MAP3K) downstream of TNFR, IL1R and Toll like receptors. It is maintained in an inactive complex with ABIN-2 (A20-binding inhibitor of NF-κB 2) and p105, and is released upon activation. TPL2 activation is a critical node of the inflammatory response with activation leading to changes in inflammatory gene transcripts via ERK1/2 and p38 activation, resulting in amplification of inflammatory responses in peripheral immune cells (Xu et al., 2018). Preclinical studies using genetic manipulation of TPL2 in mice have found that TPL2 deficiency provides beneficial effects in multiple inflammatory disease models, such as inflammatory bowel disease (IBD), Psoriasis, Pancreatitis and Multiple sclerosis (Senger et al., 2017; Sriskantharajah et al., 2014; Xiao et al., 2014; Xu *et al.*, 2018), and TPL2 is being pursued as a target for treating inflammatory conditions including RA and psoriasis (Zarrin et al., 2021).

To evaluate a potential role for TPL2 kinase activity in microglia during neuroinflammation, we used TPL2 inhibitors and TPL2 kinase dead (TPL2-KD) mice (D270A mutation). TPL2-KD mice were chosen instead of TPL2 knockout (KO) mice because TPL2 is required to maintain stable expression of its interacting partner ABIN-2 and TPL2 KO mice have dramatically reduced ABIN-2 levels, which could confound interpretations regarding the role of TPL2 kinase activity (Sriskantharajah *et al.*, 2014; Webb et al., 2019). We first examined the function of TPL2 in microglial inflammation using *in vitro* models, then in acute neuroinflammation settings, and finally in a tauopathy model of chronic neurodegeneration. These experiments indicate that TPL2 regulates microglia inflammatory activity and damage to neurons, and that blocking TPL2 function can be neuroprotective. Measurement of the cellular changes that occurred in the brains of the tauopathy mouse model with TPL2-KD along with reduced neurodegeneration and normalization of behavior reveal multiple potential beneficial aspects of preventing TPL2 kinase activity.

Results

TPL2 modulates inflammatory responses of microglia

TPL2 is expressed in both innate and adaptive immune cells in the peripheral immune system to regulate inflammatory responses (Xu *et al.*, 2018). To examine the expression of TPL2 in the brain under resting and disease conditions, we analyzed published datasets as well as datasets we recently generated. RNA-seq analysis of FACS purified cells from human (Srinivasan et al., 2020) and mouse (Zhang et al., 2014) cortex revealed that TPL2 expression is enriched in brain myeloid cells

(supplementary Fig. S1A). In an acute neuroinflammation study, in which mice received intraperitoneal injection of the endotoxin lipopolysaccharide (LPS), TPL2 expression was highly induced in both bulk brain tissue (GSE196401) and sorted microglia (Srinivasan et al., 2016). We also found that TPL2 gene expression was upregulated in bulk tissue (GSE186414) and sorted microglia from the P301S Tauopathy mouse model (Friedman et al., 2018) (supplementary Fig. S1B). Western blot analysis of TPL2 protein levels in the cortex of Alzheimer's disease (AD) patients showed an increase compared to healthy control brains (supplementary Fig. S1C).

We first used mouse primary microglia cultures to investigate the TPL2 signaling cascade in this brain cell type. Upon LPS stimulation, phosphorylation of ERK and p38 was dramatically increased, and this increased phosphorylation was significantly dampened in the presence of the TPL2 small molecule inhibitors G-767 and G-432 (Fig. 1A,B; supplementary Fig. S2A). In contrast, as expected, LPS-induced nuclear factor-kappa B (NF-κB) pathway activation, as measured by elevation of phospho-p65, was not affected by TPL2 inhibition. Of note, the TPL2 inhibitors did not affect baseline phosphorylation of ERK, p38 or p65 without stimulation (Fig. 1A,B). These results are consistent with TPL2 mediating mitogen-activated protein kinase (MAPK) signaling, but not NF-κB signaling, in microglia. It is well established that TPL2 plays an important role in regulating cytokine production by myeloid cells in the peripheral immune system via the MAPK signaling pathway (Arthur and Ley, 2013). Consistently, using multiplex immunoassays to measure cytokine release by microglia, we found that LPS induced production of inflammatory cytokines, such as TNFα, IL-1α, IL-6 and CXCL1, was greatly reduced in the presence of TPL2 inhibitors (Fig. 1C and supplementary Fig. S2B, S3A). Moreover, when we analyzed cytokine release by microglia cultured from TPL2 kinase dead (KD) mice, there was dramatically decreased LPS-induced cytokine production (Fig. 1D and supplementary Fig. S3B). Overall, this data indicates that TPL2 is a key regulator of the microglial MAPK signaling pathway and proinflammatory cytokine responses, and thus could play an important role in modulating neuroinflammation in the brain.

Inhibition of TPL2 kinase activity protects against neuronal death in a co-culture model

Activated microglia can be neurotoxic by releasing factors such as proinflammatory cytokines and reactive oxygen species (ROS) (Glass et al., 2010; Wang et al., 2015). Since we found that TPL2 can modulate proinflammatory responses in microglia, we next examined if targeting TPL2 could dampen neurotoxic functions of activated microglia. To investigate this, we used an *in vitro* microglia and neuron co-culture system and tested pharmacological and genetic inhibition of TPL2 kinase activity. Stimulation of microglia and neuron co-cultures with LPS + interferon gamma

(IFNγ), a stimulus reported to induce strong microglia activation (Straccia et al., 2011), resulted in almost complete neuronal loss as measured by MAP2 immunostaining (Fig. 2A,B). Strikingly, when the TPL2 inhibitor G-767 was added to the co-culture, the neuronal loss induced by the LPS + IFNγ stimulation was nearly fully rescued. In addition, when WT neurons were co-cultured with microglia isolated from TPL2-KD mice, stimulation-induced neuronal loss was also rescued (Fig. 2A,B). Of note, when neurons were cultured alone and stimulated with LPS + IFNγ or co-cultured with microglia at 1:1 ratio without stimulation, no obvious neuronal loss was observed (supplementary Fig. S4).

We next wanted to understand the mechanism of neuronal death and the neuroprotective effect of TPL2 kinase inhibition in this co-culture system. Several groups have shown that LPS + IFNγ stimulation can induce dramatic increases of inducible nitric oxide synthase (iNOS) expression in microglia and subsequent release of nitric oxide (NO), which is neurotoxic (Papageorgiou et al., 2016; Sheng et al., 2011; Straccia *et al.*, 2011). Consistent with this mechanism, we found that when primary microglia cultures were stimulated with LPS + IFNγ, iNOS protein levels were increased and accumulated over time (Fig. 2C,D). TPL2 small molecule inhibition significantly reduced iNOS protein in stimulated microglia (50% reduction) and stimulated microglia isolated from TPL2-KD mice also showed a dramatic reduction of iNOS (85% reduction) (Fig. 2C-E). To determine if NO plays a role in neuronal death in the co-cultures, we utilized the iNOS inhibitor 1400W. Treatment with the iNOS inhibitor almost fully rescued the neuronal loss (Fig. 2F,G), indicating that NO production by activated microglia is a key contributor to neuronal death in this co-culture system.

TPL2 reduces acute neuroinflammation in an *in vivo* LPS injection model

We next examined the role of TPL2 *in vivo* using an acute neuroinflammation model. We injected WT or TPL2-KD mice with either PBS or LPS (10 mg/kg i.p.) and collected brain tissue 24 hours later for bulk RNA-seq analysis. Using previously defined CNS myeloid gene modules (Friedman *et al.*, 2018), we found that LPS induced significantly increased expression of disease associated microglia (DAM) genes (e.g., *Il1r1*, *Axl*) in WT mice, whereas this microglia activation response was attenuated in LPS treated TPL2-KD mice (Fig. 3A,D,E). Homeostatic microglia gene expression (e.g., *Tmem119*, *Cx3cr1*) was downregulated by LPS in WT mice, but relatively unchanged in LPS treated TPL2-KD mice (Fig. 3C,D,E), consistent with TPL2-KD microglia being in a less activated state after stimulation. Interestingly, an increase in microglia proliferation genes by LPS in WT mice was also normalized in TPL2-KD mice (Fig 3E).

In addition to directly affecting neurons, microglia have also been shown to indirectly cause neurotoxicity by activating astrocytes. Cytokines released by microglia in response to LPS stimulation can induce the transition of astrocytes from a resting state to an activated/reactive state that can be neurotoxic (Liddelow *et al.*, 2017). Consistent with a reduction of microglia activation of astrocytes, LPS-induced activated astrocyte gene expression (e.g., *Cd44, Srgn*) was also attenuated in TPL2-KD mice (Fig. 3B,D,E). In parallel to the RNAseq measurements, we also measured brain cytokine levels and found that several cytokines such as IL-1α, IL-6, and CXCL1 that were elevated in LPS treated WT mouse brains, had significantly lower levels in TPL2-KD mouse brains (Fig. 3F). Collectively, these results indicate TPL2 plays a key role in microglia and astrocyte activation *in vivo*, and show that acute neuroinflammation can be reduced by ablation of TPL2 kinase activation.

We next investigated if TPL2 kinase deficiency could protect against neuronal damage in acute injury models. We first tested the mouse optic nerve crush (ONC) model. However, although we observed moderate reduction of microgliosis in TPL2-KD mice after ONC, we did not see rescue of retinal ganglion cell loss, (supplementary Fig. S5A). Additionally, we also investigated the role of TPL2 in another acute model, the rat transient middle cerebral artery occlusion (tMCAO) model of stroke. Similarly, despite significantly reduced microgliosis, we did not see beneficial effects in TPL2-KD rats in terms of body weight loss, behavioral deficits and lesion volume measured by MRI after tMCAO (supplementary Fig. S5B-H). These results highlight that reduced neuroinflammation with TPL2KD may not be sufficient for neuroprotection in cases of severe acute tissue damage.

Neuroinflammation in TauP301S tauopathy model is attenuated in TPL2-KD mice

To determine if TPL2 contributes to neuroinflammation and neurodegeneration in a chronic disease setting, we crossed TPL2-KD mice with TauP301S tauopathy mice. These transgenic mice overexpress human mutant Tau and develop pathology marked by phosphoTau accumulation, neuroinflammation and brain atrophy as the mice age, especially in the hippocampus (Wu *et al.*, 2019; Yoshiyama et al., 2007). We examined astrogliosis and microgliosis by analyzing the microglia marker Iba1 and the astrocyte marker GFAP in 9-month-old male mice and 11-month-old female mice, as female mice develop the Tau pathology slower compared with the male mice in this mouse line based on our previous experience (Wu *et al.*, 2019). TPL2KD did not affect the % area of the brain covered by Iba1 or GFAP in non-transgenic mice. In TauP301S mice, the Iba1 and GFAP signals were greatly increased reflecting gliosis, and TPL2 kinase deficiency slightly ameliorated this gliosis (Fig. 4A,B). The effect was observed with either whole brain section

analysis or hippocampal region analysis. Interestingly, phospho-Tau pathology (measured by AT8 staining) was also somewhat reduced in TauP301S;TPL2KD mice (Fig. 4A,B), potentially reflecting the interplay between neuroinflammation and Tau pathology (Didonna, 2020; Maphis et al., 2015). Consistent with the gliosis changes, the levels of several cytokines and chemokines that were significantly increased in TauP301S mouse brains were blunted in TauP301S;TPL2KD brains, including CXCL9, CXCL10, IL6 and IFNγ (Fig. 4C).

Single-cell RNA-seq analysis reveals reduced peripheral immune cell infiltration in P301S;TPL2KD mice

To gain further insight into the effect of TPL2-KD in the P301S brain, we performed single-cell RNA sequencing of the hippocampus, a brain region where pathology is most prominent in the TauP301S model. Dimensional reduction by Seurat clustering and interpretation of clusters using previously established gene sets (Friedman *et al.*, 2018; Lee et al., 2021b; Zeisel et al., 2018) resulted in annotation of 13 cell types (Fig. 5A, supplementary Fig. S6, Table S1). To investigate how Tau pathology and TPL2 kinase activity affected the relative abundance of various cell types, we examined cellularity across genotypes (Fig S7). P301S mice showed increases in relative abundance of several cell types (supplementary Fig. S6B, S7), including microglia, T cells, and a cluster we initially labeled as "mixed immune cells" (Fig. 5A, and supplementary Fig. S7). Further analysis of the mixed immune cells cluster showed that it contained a unique cell type with expression of distinct genes compared to microglia or T cells (e.g. *Plbd1, Mgl2, Clec9a*) (supplementary Fig. S8A). Subclustering of the mixed immune cells identified this unique cell type as a distinct cluster from microglia or T cells (supplementary Fig. S8), and mapping onto ImmGen cell type data (Heng et al., 2008) revealed this population corresponded to dendritic cells (supplementary Fig. S8). Like microglia and T cells, dendritic cells also showed an elevation in P301S brains (Fig. 5C; supplementary Fig. S9). Strikingly, while TPL2KD did not have a significant effect on the proportion of any of the 13 cell types in non-transgenic mice, and did not alter the proportion of most cell types in P301S brains, TPL2KD significantly reduced the abundance of T cells and dendritic cells in P301S brains (Fig. 5B,C; supplementary Fig. S9). This indicates P301S;TPL2KD mice have reduced infiltration of peripheral immune cells compared to P301S mice. Given the presence of T cells in the brains of human AD patients and preclinical disease models, and the beneficial effects of T cell depletion in mouse disease or injury models (Gate *et al.*, 2020; Laurent *et al.*, 2017; Merlini *et al.*, 2018; Togo et al., 2002), the decreased presence of peripheral immune cells in TauP301SxTPL2KD mouse brains could have beneficial effects.

Subclustering of the T cells identified 2 clusters of CD4+ (CD4.1-2) cells and 4 clusters of CD8+ cells (CD8.1-4), with CD8+ cells being the dominant T cell population (Supplementary Fig. S10A,B). Cellularity analysis showed that both CD4+ and CD8+ cell numbers were increased in P301S brains, and TPL2KD significantly reduced the abundance of both cell types (Supplementary Fig. S10C). When the relative abundance was compared within the T cell population, CD8.4, the largest T cell subcluster, was decreased in P301S;TPL2KD mouse brains (supplementary Fig. S10D). CD8.4 cells expressed some marker genes of exhausted T cells, such as *Nr4a2* and *Pdcd1*, which are usually induced by chronic/persistent exposure to antigens and/or inflammation (Odagiu et al., 2020; Wherry, 2011; Wherry and Kurachi, 2015; Yi et al., 2010).

Normalization of microglial gene expression changes in P301S;TPL2KD mice

To investigate the genotype-dependent gene expression changes in various cell types, we performed pseudo-bulk analysis for each cell type in this study (Fig. S11). Comparing TauP301S with non-transgenic mice, there were many differentially expressed genes (DEGs) across multiple cell types, such as astrocytes, microglia and oligodendrocytes (Fig. S11A). However, within the TauP301S group, when comparing TPL2-KD to TPL2-WT mice, DEGs were only detected in microglia (Fig 6A), consistent with TPL2 being most highly expressed by microglia in the mouse brain (supplementary Fig. S1). Analysis of the protein coding DEGs showed that the most upregulated genes in P301S microglia were consistently upregulated to a lesser extent in P301S;TPL2KD microglia, including cytokines like *Tnf* and multiple immediate early genes (IEGs) such as *Egr1* (Fig. 6B,C).

To further analyze microglia phenotypes, the ~55,000 microglia in the study were sub-clustered into 22 clusters (Fig. 6D). As expected, clusters of microglia annotated as neurodegeneration-related and interferon-related were elevated, and clusters annotated as resting/homeostatic were decreased in TauP301S mice (supplementary Fig. S11, S12). However, the abundance of these clusters in P301S mice were not altered by TPL2KD (supplementary Fig. S11, S12). On the other hand, a subcluster of microglia (C11) expressing high levels of IEGs (e.g. *Fos, Egr1-3, Atf3*) (supplementary Fig. S11E), was elevated in P301S mice, and this elevation was ameliorated by TPL2KD (Fig 6E). Calculation of IEG gene set score for every defined cell type (pseudo-bulk) showed IEG expression was up in astrocytes, microglia, oligodendrocytes, OPCs and VSMCs, but the upregulation was only normalized by TPL2-KD in microglia (and to some extent in VSMCs, although not statistically significant, supplementary Fig. S11G). As IEG expression can be regulated by MAPK signaling pathways and TPL2 is a key regulator of MAPK signaling(Bahrami and Drablos, 2016; O'Donnell et al., 2012), these results are consistent with a

specific role for TPL2 in TauP301S microglia. Another subcluster of microglia (C20) that was elevated in P301S and normalized by TPL2KD in the P301S mice expressed high levels of MHC (major histocompatibility complex) class II genes (e.g. *Cd74, H2-Aa, H2-Ab1*, etc.), which are usually expressed by antigen presenting cells (APCs) and are important for the generation of immune responses via interaction with T cells (Neefjes et al., 2011; Roche and Furuta, 2015) (Fig 6F, supplementary Fig. S11F). The reduction of P301S MHCII expressing microglia by TPL2KD in P301S mice combined with the reduction of infiltrating T cells and dendritic cells points to a normalization of adaptive immune function in P301S brains.

TPL2KD ameliorates dendritic spine loss and brain atrophy in TauP301S mice

Given that TPL2KD provided neuroprotection *in vitro,* decreased gliosis, immune cell infiltration, and altered microglia states in P301S mice, we next asked if TPL2KD provides neuroprotection in P301S mice. As microglia-mediated synapse elimination has been observed in AD mouse models including P301S mice (Hansen *et al.*, 2018; Stephan et al., 2012; Wilton et al., 2019), we quantified synapse density by measuring spine number in sparsely labeled dendrites using GFP expression driven by the Thy1-GFP-M transgene. Spine analysis by *ex vivo* imaging found that P301S;TPL2KD mice had significantly increased spine density compared to P301S mice (Fig. 7A), consistent with potentially reduced microglia removal of spines in P301S;TPL2KD mice.

Previous studies have shown that TauP301S mice develop neurodegeneration, including ventricle enlargement and brain volume reduction, that can be measured by volumetric MRI (vMRI) (Dejanovic *et al.*, 2018; Wu *et al.*, 2019). We next investigated if TPL2-KD could protect against neurodegeneration in tauopathy mice using longitudinal vMRI. In WT mice, ventricle volumes stayed stable and neocortex and whole brain volumes increased between 6 and 9 months, and TPL2 kinase deficiency did not alter the trajectory of the brain volume changes. As expected, P301S mice developed brain atrophy, as indicated by increasing ventricle volumes and decreasing brain volumes between 6 and 9 months. Strikingly, TPL2KD significantly ameliorated the ventricle enlargement and brain volume decline in TauP301S mice (Fig. 7B,C), indicating a robust neuroprotective effect of inhibition of TPL2 kinase activity in this mouse model. We also measured plasma NfL (neurofilament light chain) to see if this potential biomarker of neurodegeneration was reduced in parallel with the protection against brain volume loss. However, while plasma NfL was strongly increased in P301S mice, TPL2KD did not significantly affect NfL levels (Fig. 7D). This indicates that while plasma NfL increases in P301S mice, neuroprotection can be achieved irrespective of NfL levels.

TPL2KD normalizes behavioral hyperactivity and memory deficits in TauP301S mice

We next evaluated if the significant attenuation of neuroinflammation and neurodegeneration by TPL2 kinase ablation in tauopathy mice resulted in functional benefits. We first examined locomotor activity in an open field. As previously seen (Dejanovic *et al.*, 2018; Wu *et al.*, 2019), compared with WT mice, 9-month-old TauP301S mice displayed behavioral hyperactivity as indicated by significantly increased total beam breaks, ambulatory bouts and rearing behavior. TPL2 kinase activity deficiency did not impact the locomotor activity of non-transgenic mice, but prevented the hyperactivity in the tauopathy mice (Fig. 7E). To assess the learning and memory functions of these mice, we performed the trace fear conditioning test, a memory test requiring both hippocampus and cortex function (Burman et al., 2014; Han et al., 2003; Sharma et al., 2018). Mice were trained to associate aversive shock with a neutral auditory tone stimulus. When tested 24 hours later, WT mice exhibited elevated freezing behavior in response to the auditory stimulus as expected. P301S mice had somewhat elevated baseline freezing behavior, and failed to exhibit an increase in freezing behavior in response to the auditory stimulus, indicating potential learning and memory deficits. In contrast, P301S;TPL2KD mice showed normal baseline freezing behavior and elevated freezing behavior in response to the tone stimulus (Fig. 7F). Thus, in addition to reducing neuroinflammation, and protecting against synapse and neuron loss, eliminating TPL2 kinase activity rescues behavioral alterations in P301S mice.

Discussion

Multiple aspects of neuroinflammation have been implicated in both preclinical AD models and AD patient brains, and studies with inhibition of specific neuroinflammation pathways have shown beneficial effects in tauopathy and AD models (Dejanovic *et al.*, 2018; Gate *et al.*, 2020; Heneka *et al.*, 2013; Hong *et al.*, 2016; Ising *et al.*, 2019; Laurent *et al.*, 2017; Liddelow *et al.*, 2017; Merlini *et al.*, 2018; Ndoja et al., 2020; Wu *et al.*, 2019). Here we focused on TPL2 which, as a master regulator of the peripheral immune system that is expressed by microglia, could have pleiotropic effects on neuroinflammation. *In vitro* studies show that similar to its function in the peripheral immune system, TPL2 is also key regulator of microglia in the brain. Pharmacological or genetic inhibition of TPL2 reduced cytokine release and iNOS induction by stimulated microglia in culture and rescued neurodegeneration in a co-culture model. TPL2KD mice also exhibited strongly ameliorated microglia and astrocyte activation and brain cytokine levels following acute peripheral LPS challenge *in vivo*.

Based on the potentially beneficial effects of reduced TPL2 kinase function in response to direct stimuli *in vitro* and *in vivo*, we tested the effects of TPL2KD in *in vivo* neurodegeneration

models. That TPL2KD lessened gliosis but did not provide neuroprotection in optic nerve crush and stroke models is perhaps not surprising given the direct severe neuronal damage in these models of acute injury. In contrast the beneficial effects in the TauP301S mice indicate that modulating immune cell function via eliminating TPL2 kinase activity can be beneficial in a context with chronic neuroinflammation where neurodegeneration gradually occurs over time. This fits with a general model of neuroinflammation in chronic neurodegenerative conditions, where an initial pathology (in this case Tau) results in glial cell activation, and over time activated glial cells contribute to neuronal damage. The partial rescue of brain volume loss in TauP301S mice with TPL2KD likely corresponds to protection of stressed but functional brain tissue that is being destroyed by the inflammatory response to Tau pathology in the brain. Consistent with this, NfL levels are not rescued with TPL2KD, which could reflect ongoing NfL production by the protected brain tissue. At the same time it is clear that despite ongoing stress from transgenic Tau production, the increased synapse density and brain volume represent preservation of functional neuronal circuits, as the behavioral phenotypes in P301S were rescued in P301S;TPL2KD mice, indicating functional benefits.

The tauopathy model study reveals multiple aspects of pathophysiology that are normalized by TPL2KD concordant with rescue of neurodegeneration and behavior. This includes reductions of the levels of various cytokines, normalization of increased T cell and dendritic cell abundance in the brain, and reduction in the IEG and MHCII subpopulations of activated microglia. This points to future avenues of research examining which features are of particular importance in the protective effects of TPL2KD. For example, do specific cytokines play critical roles in pathophysiology? Is an aberrant role for adaptive immunity in the brain critical to degeneration? Are changes in subpopulations of activated microglia critical? Or are the pleiotropic effects of TPL2 kinase deficiency in combination required for benefit?

Microglia orchestrate both protective and damaging responses during neurodegeneration in conditions such as Alzheimer's disease (Bohlen et al., 2019; Hansen *et al.*, 2018). While our results support a beneficial role of reducing microglia activation by inhibiting TPL2, other recent therapeutic approaches have focused on boosting microglia activation to accelerate clearance of disease related protein aggregates, such enhancing TREM2-mediated, stimulation of microglia phagocytosis of Aβ (Fassler et al., 2021; Wang et al., 2020). Thus, TPL2 inhibition to reduce the harmful aspects of microglia-mediated inflammation could potentially be combined with other approaches to boost beneficial effects of microglia activation.

Overall, our data indicate that reducing the inflammatory state of the brain with approaches such as targeting TPL2 kinase activity could be a potential therapeutic approach for diseases with

chronic neuroinflammation. Our data also highlight various TPL2-dependent features of neuroinflammation include elevated brain cytokine levels peripheral immune cell infiltration, specific activation states of microglia, etc. that could be explored as other potential therapeutic approaches.

Materials and methods

Animal Use

All rodent experiments were approved by the Genentech Animal Care and Use Committee and followed the National Institutes of Health *Guide for the Care and Use of Laboratory Animals*.

Rodent models

All rodent experiments were approved by the Genentech Animal Care and Use Committee and followed the National Institutes of Health *Guide for the Care and Use of Laboratory Animals*. TauP301S mice expressing human Tau with the P301S mutation, driven by the PrP promoter (Yoshiyama *et al.*, 2007) were crossed to TPL2 kinase-deficient mice carrying D270A mutation generated in-house (Senger *et al.*, 2017). All TauP301S mice were heterozygous for the TauP301S transgene and all TPL2-KD mice were homozygous for the TPL2-D270A mutation. For the stroke study, TPL2 kinase-deficient rats carrying D270A mutation generated by Genentech were used. Cohorts were produced with all genotypes as littermates. Experimenters were blind to genotype for all behavioral measurements, microscopic, and histological analyses.

Human post mortem brain tissue

Post mortem brain tissue (superior frontal gyrus) was obtained from patients with putative AD as indicated by cognitive evaluation scores (‘‘EAD’’) or pathology-confirmed AD (‘‘AD’’) along with age-matched controls from Folio Biosciences. Human samples were procured with Ethics Committee approval and written informed consent. Adult male and female patients aged 63-93 years were used in this study.

Immunoblotting

Cells were directly lysed in 2x reducing SDS sample buffer. Mouse brain tissues were homogenized in cold RIPA buffer (50 mM Tris-HCl, 150 mM NaCl, 2 mM EDTA, 1% NP-40, 0.1% SDS) supplemented with phosphatase and protease inhibitors, using a TissueLyser (2 × 30 Hz, 3 min at 4°C; QIAGEN). After homogenization, samples were centrifuged at 20,000 g for

20 min and the supernatants were transferred into new tubes. The supernatants were then boiled in reducing SDS sample buffer. For human brain tissues, after homogenization in RIPA buffer, SDS loading buffer (final 1.5x) without bromophenol blue/DTT was added to the lysates and the lysates were sonicated. Then the lysates were boiled for 5 min and centrifuged at 15,000 rpm for 15 min. The supernatants were collected. After protein concentrations were measured using BCA reagents (Thermo Fisher), bromophenol blue and DTT were added to the supernatants. The protein samples were separated by Novex Tris-Glycine SDS-PAGE gels (Invitrogen) and transferred to nitrocellulose membranes (Bio-Rad). Membranes were then blocked with 5% milk in TBST or Licor blocking buffer for one hour (RT) and incubated with primary antibodies (in 5% milk or 2% milk in TBST or Licor blocking buffer with 0.1% Tween20, 4ºC overnight), and then secondary HRP-conjugated antibodies (two hours RT). Chemiluminescence signals were detected on ChemiDoc (Bio-Rad). Data analysis was done using Image Lab software (Bio-rad). Antibodies used for western blots are: anti-ERK(1/2) (#9102S; RRID: AB_330744), anti-phospho-ERK (Thr202/Tyr204) (#4370S; RRID: AB_2315112), anti-p38 (#9212S; RRID: AB_330713), anti-phospho-p38 (Thr180/Tyr182) (#9211S; RRID: AB_331641), anti-NF-κB p65 (#8242S; RRID: AB_10859369), anti-phopho-NF-κB p65 (Ser536) (#3033S; RRID: AB_331284), anti-iNOS (clone D6B6S, #13120S; RRID: AB_2687529), anti-β-Actin (#4970S; RRID: AB_2223172). The above antibodies are all from Cell Signaling Technology, Danvers, MA, USA. TPL2 antibody is from Santa Cruz Biotechnology (sc-373677; RRID: AB_10915433). Calnexin antibody is from Enzo lifesciences (#ADI-SPA-865-F; RRID: AB_11180747).

Neuron and microglia co-culture assay

Mouse embryonic cortical neurons were cultured as described previously (Friedman *et al.*, 2018). Briefly, cortices from day 15 C57BL/6N embryos (E15) were dissected and washed thrice with pre-cooled Hank's balanced salt solution (HBSS; Invitrogen). Cortical tissue was incubated for 10 minutes at 37°C in HBSS supplemented with 0.25% trypsin (Invitrogen, CA, USA) and DNase I (Roche CustomBiotech, IN, USA). Tissue was washed thrice with cold HBSS and triturated in plating media containing DNAse I (Gibco Neurobasal Medium (Thermo Fisher Scientific, MA, USA), 20% heat-inactivated horse serum (Thermo Fisher Scientific), 25 mM sucrose, and 0.25% Gibco GlutaMAX (Thermo Fisher Scientific)). Dissociated cells were centrifuged at 125 *g* for 5 minutes at 4 °C. Cells were resuspended in the plating medium and plated on Poly-D-Lysine and laminin coated glass coverslips in 24-well plates (180k/well). After ~2 hours, the plating medium was replaced with NbAct4 culture medium (Brainbits). Cells were maintained

in an incubator at 37°C with 5% CO_2 and the medium was renewed using 50% exchange every 3-4 days to maintain cell health.

Primary microglia were cultured from P0-P2 pups as previously described(Yeh et al., 2016). Briefly, mouse brains were dissected out and the brain tissue was disrupted by trituration using a 10 mL serological pipette in cold DMEM media. The homogenate was spun at 300 g for 5 min. The pellet was resuspended in DMEM media and filtered through a 70 μm cell strainer. Dissociated cells were cultured in 175 cm^2 flasks with media containing DMEM, 10%FBS and 1% penicillin/streptomycin. Flasks were rinsed with PBS and new media was added after 24 h. After ~12 days, microglia were shaken off (125rpm for 1hr), collected and added to one-week-old or two-week-old mouse cortical neuronal cultures at 1:1 cell number ratio. After 3 hrs, neuron and microglia co-cultures were stimulated with 25 ng/mL or 100 ng/mL LPS and 30 ng/mL interferon gamma. One day after stimulation (one-week-old neuron culture) or 3 days after stimulation (two-week-old neuron culture), cultures were fixed with 4% PFA for 10 min, rinsed with PBS, blocked with 10% goat serum with 0.1% Triton X-100 in PBS, incubated with primary antibodies (in block solution, 4°C, overnight), and then secondary antibodies (in block solution, RT, 1 hr). After staining, cells were mounted using Prolong Diamond Antifade Mountant with DAPI (Thermo Fisher). Primary antibodies used for immunostaining are: anti-MAP2 (Sigma-Aldrich, MO, USA, #M9942; RRID: AB_477256), anti-Iba1 (synaptic systems, #234 004; RRID: AB_2493179). Cells were imaged with a confocal laser scanning microscope LSM710 (Carl Zeiss) using Zen 2.3 SP1 software (Carl Zeiss). Maximum intensity projection images were created using ImageJ. Immunostainings were analyzed using MATLAB software.

Cytokine measurements

For primary microglia culture, after 24 hrs incubation with LPS (100 ng/mL) or vehicle control, culture supernatants were collected and cytokine levels in the samples were measured using a Bio-Plex Pro Mouse Cytokine 23-Plex Assay (Bio-Rad).

For in vivo studies, following perfusion with PBS, whole hemi brains (LPS i.p. injection study) or hippocampi (TPL2xTauP301S study) were isolated and homogenized in cold RIPA buffer as described above for preparation of immunoblotting samples. The protein concentration in each sample (supernatants after centrifugation) was measured by BCA (ThermoFisher). Cytokine levels in the samples were measured using mouse cytokine 23-Plex Assay (Bio-Rad) or mouse cytokine 32-Plex Assay (Millipore) and normalized to total protein concentration.

Bulk RNA-seq

~3-month-old WT or TPL2-KD mice were injected with PBS vehicle control or LPS (10 mg/kg) (n =5 per condition). 24 hours later, mice were perfused with cold PBS and the mouse hemi brains were immediately sub-dissected and preserved in RNAlater. RNA was extracted from samples using Qiagen RNeasy Plus Mini Kit. Concentration of RNA samples was determined using NanoDrop 8,000 (Thermo Scientific) and RNA integrity was determined by Fragment Analyzer (Advanced Analytical Technologies). 0.5 µg of total RNA was used as an input material for library preparation using TruSeq RNA Sample Preparation Kit v2 (Illumina). Library size was confirmed using a Fragment Analyzer (Advanced Analytical Technologies). Library concentrations were determined by qPCR-based using a Library quantification kit (KAPA). The libraries were multiplexed and then sequenced on Illumina HiSeq2500 (Illumina) to generate 30 M of single end 50 base pair reads per library(Srinivasan *et al.*, 2016).

The fastq sequence files for all RNA-seq samples were filtered for read quality (keeping reads where at least 70% of the cycles had Phred scores ≥ 23), and ribosomal RNA contamination. The remaining reads were aligned to the mouse reference genome (GRCm38) using the GSNAP alignment tool(Wu and Nacu, 2010). These steps, and the downstream processing of the resulting alignments to obtain read counts were implemented in the Bioconductor package HTSeqGenie (https://bioconductor.org/packages/release/bioc/html/HTSeqGenie.html). Only uniquely mapped reads were used for further analysis. Differential gene expression analysis was performed with voom+limma(Law et al., 2014).

For heatmaps (Fig. 3A-C), gene expression data were first normalized to nRPKM statistic as described (Law *et al.*, 2014), then transformed to a log2 scale. Any values less than -40 XX were then replaced by 40, and standard Z-score calculation was performed (for each gene, subtracting mean and dividing by standard deviation) and then used for visualization.

Gene set scores were calculated as previously described (Friedman *et al.*, 2018). Briefly, gene expression values were first transformed (and stabilized) as log2(nRPKM+1). The gene set score for a sample was then calculated as the average over all genes in the set of log-transformed expression values.

Single cell RNAseq

9-month-old WT (n = 3), TPL2KD (n = 3), P301S (n = 6), or P301S;TPL2KD (n = 6) mice were perfused with cold PBS and the hippocampi were immediately sub-dissected. Single cell suspensions were prepared from the hippocampi as described (Lee et al., 2021a). Briefly, hippocampi were chopped into small pieces and dissociated with enzyme mixes in a Neural Tissue Dissociation Kit (P) (Miltenyi 130-092-628) in the presence of actinomycin D. After dissociation,

cells were resuspended in Hibernate A Low Fluorescence medium (Brainbits) containing 5% FBS, with Calcein Violet AM (Thermo Fisher C34858) and propidium iodide (Thermo Fisher P1304MP). Flow cytometry was used to sort and collect live single-cell suspensions for the single-cell RNAseq study.

Sample processing and library preparation was carried out using the Chromium Single Cell 3′ Library and Gel Bead Kit v3 (10X Genomics) according to manufacturer's instructions. Cell-RT mix was prepared to aim 10,000 cells per sample and applied to Chromium Controller for Gel Bead-in-Emulsion (GEM) generation and barcoding. Libraries were sequenced with HiSeq 4000 (Illumina). Single-cell RNA sequencing data were processed with an in-house analysis pipeline as described (Lee *et al.*, 2021a; Yartseva et al., 2020). Reads were demultiplexed based on perfect matches to expected cell barcodes. Transcript reads were aligned to the mouse reference genome (GRCm38) using GSNAP (2013-10-10) (Wu and Nacu, 2010). Only uniquely mapping reads were considered for downstream analysis. Transcript counts for a given gene were based on the number of unique UMIs (up to one mismatch) for reads overlapping exons in sense orientation. Cell barcodes from empty droplets were filtered by requiring a minimum number of detected transcripts. Sample quality was further assessed based on the distribution of per-cell statistics, such as total number of reads, percentage of reads mapping uniquely to the reference genome, percentage of mapped reads overlapping exons, number of detected transcripts (UMIs), number of detected genes, and percentage of mitochondrial transcripts. After this primary analysis step, cells with less than 1,000 total UMIs or greater than 10% mitochondrial UMIs were discarded. UMI normalization was performed by dividing each gene expression value for a cell by a factor proportional to the total number of transcripts in that cell. More precisely put, letting n_c represent the total number of UMIs for cell c, then the normalization factor fc for that cell was given by

$$f_c = \frac{n_c}{median_{c'}(n_{c'})}$$

(with c′ going over all cells) and the "normalized UMIs" for gene g and cell c given by $nUMI_{g,c} = n_c / f_c$.

Seurat (Stuart et al., 2019) was used to calculate PCA, tSNE coordinates and Louvain clustering for all cells (Figures 5A, 6D, S8B). Cell type markers from (Friedman *et al.*, 2018; Zeisel *et al.*, 2018) were used to identify major cell type clusters, and were interpreted using marker gene sets (Figures 5A, S6, S8B). Color scales in individual gene tSNE plots indicate gene expression on a log2 scale (log2(normCount+1)). All gene sets used in this study are available in Table-S1.

T cells were extracted from the dataset, re-normalized and the 3,000 most variable genes were identified. Dimensionality reduction on the variable genes was performed using principal

component analysis and the top 30 principal components (PCs) were used as input to Louvain graph-based clustering and UMAP dimensionality reduction. T cell subtypes were identified based on the marker genes: *Cd3e*, *Cd4*, and *Cd8a*. Additional marker genes were determined using the *scoreMarker* function of the Bioconductor package scran (Lun et al., 2016).

A cluster of doublets, co-expressing microglia and T-cell genes, and a cluster of T cells, only present in two animals and enriched for ribosomal proteins, were identified and excluded from downstream analyses.

T-cell subtype percentages were calculated for each sample either as a percentage of the total number of cells in a sample or as a percentage of the total number of T cells in a sample.

Pseudo-bulk of various cell type expression profiles were derived from single-cell datasets first by aggregating each sample's data for each cell type as described (Lee *et al.*, 2021a; Lee *et al.*, 2021b). So, for n samples and m cell types there were n*m total possible pseudobulks (that is, aggregates of cells of a single type from a single sample). If fewer than 10 cells of a particular type were present in a given sample then they were discarded, so the actual total number of pseudo-bulks was less than n*m. A single "raw count" expression profile was created for each pseudo-bulk simply by adding the total number of UMIs for each gene across all cells of that type from that sample. This gave a gene-by-pseudo-bulk count matrix which was then normalized to a normalizedCount statistic using the estimateSizeFactors function from DESeq2 (Love et al., 2014), used for calculating gene set scores and visualizing gene expression, and for normalization factors for differential expression (DE) analysis. DE was performed on pseudo-bulk datasets using voom+limma methods for bulk RNA-seq. To put this into more formal notation, let n_{ij} be the raw UMI number of gene i in each cell type j. Let s_j indicate the sample of cell j. The pseudo-bulk count matrix B, with rows indexed by genes and columns indexed by samples (instead of cells) is defined as

$$B_{is} = \sum_{j:s_j = s} n_{ij}$$

The matrix B is then size-factor normalized and analyzed using the standard methods of bulk RNA-seq, including differential expression (DE) analysis using voom+limma (Law *et al.*, 2014). DE analysis was performed mostly as previously described (Lee *et al.*, 2021a; Lee *et al.*, 2021b; Srinivasan *et al.*, 2020) using voom+limma methods for bulk RNA-seq. For each analysis (that is, for each pair of groups of pseudobulks to be compared), low expressed genes were filtered out. This was defined as genes with at least 10 total UMIs in at least 3 of the analyzed pseudobulks. Gene set scores for each pseudo-bulk profile were calculated as described above for ScRNA-seq data, except NormCount values were used in the place of nUMI values.

Cellularity (cellular composition) plots are plotted using geom_boxplot (https://ggplot2.tidyverse.org/reference/geom_boxplot.html). The lower and upper hinges correspond to the first and third quartiles (the 25th and 75th percentiles). The upper whisker extends from the hinge to the largest value no further than 1.5 * IQR from the hinge (where IQR is the inter-quartile range, or distance between the first and third quartiles). The lower whisker extends from the hinge to the smallest value at most 1.5 * IQR of the hinge. Data beyond the end of the whiskers are called "outlying" points and are plotted individually (Cleveland and McGill, 1985). P values are based on t-test between indicated groups using ggpubr.

Ex vivo imaging analysis of dendritic spine density

9-month-old WT, TPL2KD, TauP301S or TauP301S;TPL2KD mice that also express Thy1-GFP-M transgene were euthanized, transcardially perfused with PBS, and brains were harvested. The brains were incubated for 48 hours in 4% PFA, and then washed with PBS and embedded in agarose for ex vivo imaging. Spines on apical dendrites of neurons in somatosensory cortex were imaged with a 2-photon laser scanning microscope (Prairie Technologies) using a Ti: sapphire laser (MaiTai DeepSee Spectra Physics; Newport) at 840 nm with a 60x numerical aperture 1.0 objective lens (Olympus). The image resolution is 0.1 mm/pixel across a 1024*1024-pixel field of view (FOV) using 0.5 mm Z-steps. In each mouse, 6 cells (1 dendrite/cell) were collected. A custom, semiautomated image analysis routines in MATLAB (MathWorks) was used to generate dendritic spine density. The density is calculated as the total number of spines divided by the length of the corresponding dendrite. Imaging and analysis were performed under blinded conditions.

Longitudinal Volumetric brain MRI imaging

MRI was performed on a 7T Bruker (Billerica, MA) system with a 4-channel receive-only cryogen-cooled surface coil and a volume transmit coil (Bruker, Billerica, MA). T2-weighted images were acquired with a multi-spin echo sequence: TR 5100 ms, TE 10, 20, 30, 40, 50, 60, 70, 80ms, 56 contiguous axial slices of 0.3mm thickness, FOV 19.2 mm x 19.2 mm, matrix size 256 x 128, 1 average, with a scan time of 11 min/mouse. During imaging, anesthesia for mouse was maintained at 1.5% isoflurane and rectal temperature was maintained at 37 ± 1 ^{o}C using a feedback system with warm air (SA Instruments, Stony Brook, NY). Equal number of males and females were included to detect any gender difference. The regional and voxel differences in the brain structure were evaluated by registration-based region of interest (ROI) analysis. In brief, multiple echo images were averaged and corrected for field inhomogeneity to maximize the contrast to noise

ratio and the images were analyzed based on a 20-region pre-defined in-vivo mouse atlas (http://brainatlas.mbi.ufl.edu/) that was co-registered to a study template and warped to individual mouse datasets. All the co-registration steps were performed in SPM8 (Wellcome Trust Centre for Neuroimaging, UCL, UK).

Histology

Mice were deeply anesthetized and transcardially perfused with phosphate-buffered saline (PBS). Hemi-brains were drop fixed for 48h at 4 C in 4% paraformaldehyde as previously described(Wu *et al.*, 2019). After being cryoprotected and frozen, up to 40 hemi-brains were embedded per block in a solid matrix and sectioned coronally at 30 μm (MultiBrain processing by NeuroScience Associates, NSA) before being mounted onto slides. TauP301S x TPL-KD cohort brain sections were stained for AminoCu, AT8, GFAP, Iba1, CD68 and NeuN at NSA using established protocols. Brightfield slides processed by NeuroScience Associates were imaged on the Nanozoomer system (Hamamatsu Corp, San Jose, CA, USA) at 200x magnification with a resolution of 0.46 micron/pixel. Quantification of chromogenic staining (AminoCu, NeuN, GFAP, Iba1, AT8, CD68) area was performed using grayscale and color thresholds(Brey et al., 2003) followed by morphological operations. Positive stain area was normalized to the whole brain section or manually marked up hippocampal area.

Open field Behavior

Spontaneous locomotor activity of 9-month-old males and 9-month-old females was measured with an automated Photobeam Activity System-Open Field (San Diego Instruments)(Wu *et al.*, 2019). Mice were placed individually in a clear plastic chamber (41L x 41W x 38H cm) surrounded by a locomotor frame and a rearing frame fitted with 16 x 16 infrared (IR) beams to record horizontal locomotor activity (3 cm above the floor) and vertical rearing activity (7.5 cm above the floor), respectively. The total number of beam breaks for both horizontal and vertical movements was calculated for a total of 20 min.

Trace fear conditioning

10-month-old female mice were individually placed in a fear-conditioning chamber (30 x 24 x 24 cm measured inside of the chamber) located inside of a sound-attenuating cubicle (Med Associates). Each chamber was equipped with a house light, an IR light, a speaker that was used to deliver white noise during the training and cued phases of the task, and a near-IR camera to record the movement and/or freezing of the mice. The floors of the compartments were equipped with

stainless steel metal grids that were connected to a shock generator. Hardware and data acquisition were controlled by Video-Freeze software (Med Associates).

During TFC training, the house lights were on and the metal grids served as the floor. TFC training began with 180 s of baseline recording in which the mice were allowed to explore the chamber, followed by 6 CS-US trials, each consisting of a 20 s tone (90 dB white noise) as the conditioned stimulus, followed by an 18 s trace interval, then a 2 s foot shock (0.5 mA) as the unconditioned stimulus, and finally a 30 s delay. After the 6 CS-US presentations were completed, the mice were returned to their home cage.

The TFC test was administered 24 hours following training. During TFC testing, the context of the chamber was altered by switching off the house lights, covering the grid floor with a plastic inlay, altering the shape of the chamber walls by another insert, and changing the scent of the chamber with a small amount of 1% acetic acid. Mice had 180 s of baseline recording to explore the new altered context before the CS tone used in training was presented for 20 s, followed by a 20 s trace interval and a 30 s delay. No foot shock was administered during the test. The freezing behavior of the mice during the trace intervals of the training and testing phases were recorded using a near infrared camera and the percentage time freezing was calculated using Video Freeze software (Med Associates).

Plasma NfL measurements

NfL and p-NfH were measured by Simoa platform at Quanterix, Inc, Billerica, MA, using NF-Light Advantage Kit (#103186) and pNF-heavy Discovery Kit (#102669).

Optic nerve crush model

Optic nerve crush was performed as previously described (Watkins et al., 2013). ~3-month-old WT or TPL2KD mice were used. The left eye of each animal was subjected to optic nerve crush injury via an intraorbital approach under deep anesthesia. An incision was made on the superior conjunctiva of the surgery eye, and the optic nerve was exposed. The crush injury was inflicted for 1 s using a 45º angled fine-tip forceps 1–2 mm from the eyeball. Unoperated right eyes were used as controls.

Whole-Mount retina immunohistochemistry was performed as previously described (Watkins *et al.*, 2013). Mouse eyes were collected and fixed in 4% paraformaldehyde (PFA) at room temperature for 1-2 hrs. After two washes in PBS, retinas were dissected out and permeabilized in PBST (0.5% Triton-X100) for 1 hour. The retinas were then incubated in blocking buffer (5% donkey serum and 0.5% Triton X-100 in PBS) at 4ºC overnight, followed by overnight

674 incubation at 4°C in primary antibodies, including anti-RBPMS (Phosphosolutions, #1830-
675 RBPMS) and anti-Iba1 (synaptic systems, #234 004) diluted in blocking buffer. After washing in
676 PBST for 6 hrs at 4°C (6 washes; one hour each), the retinas were incubated overnight at 4°C with
677 secondary antibodies and washed with PBST for 6 hrs. Before mounting on slides, each retina was
678 rinsed in PBS and was cut with 4-5 slits along the radial axes from the edge to about two-thirds of
679 the radius to flatten the retina and then mounted on slides. Number of RGCs and microglia were
680 counted using MATLAB software.
681
682 **Rat stroke model**
683 Rat stroke model was performed as previously described(Stark et al., 2021). All animal
684 experiments were performed as specified in the license authorized by the national Animal
685 Experiment Board of Finland (Eläinkoelautakunta, ELLA) and according to the National Institutes
686 of Health (Bethesda, MD, USA) guidelines for the care and use of laboratory animals. In total, 60
687 adult male rats (30 WT and 30 TPL2 KD) were generated through intercrossing and assigned to the
688 study at the age of ~9–10 weeks old. Transient focal cerebral ischemia was produced by middle
689 cerebral artery (MCA) occlusion in right hemisphere of brain in male rats. The rats were
690 anesthetized with 5% isoflurane. During the operation, the concentration of anesthetic was reduced
691 to 1.0–1.5%. After midline skin incision, the right common carotid artery (CCA) was exposed, and
692 the external carotid artery (ECA) was ligated distal from the carotid bifurcation. Filament with
693 silicon-covered tip (Doccol filament 4–0, dia 0,185 mm, silicon 5–6 mm/dia 0.35 mm) was inserted
694 22–23 mm into the internal carotid artery (ICA) up to the origin of MCA. Directly after occlusion,
695 animals were assessed with DWI as described below. After 90 min of ischemia, the MCA blood
696 flow was restored by removal of the thread. The wound was closed and the animals were allowed
697 to recover from anesthesia. Sham animals underwent identical procedures, including anesthesia
698 regime, but without the filament insertion and actual tMCAO.
699 Lesion size, tissue viability (T2 in milliseconds) and brain edema were determined using
700 absolute T2-MRI on days 2, 15, and 30. MRI acquisition was performed using a horizontal 7T
701 magnet with bore size 160 mm equipped with a gradient set capable of max. gradient strength
702 750 mT/m and interfaced to a Bruker Avance III console (Bruker Biospin GmbH, Ettlingen,
703 Germany) as described in(Stark *et al.*, 2021). Multi-slice multi-echo sequence was used with the
704 following parameters; TR = 2.5 s, 12 different echo times (10–120 ms in 10 ms steps) and 4
705 averages. Eighteen (18) coronal slices of thickness 1 mm were acquired using field-of-view
706 30 × 30 mm^2 and 256 × 128 imaging matrix. Blinded volumetric analysis was performed manually,
707 with lesions delineated based on the contrast differences between lesioned and healthy tissues in

the ipsilateral side taking into account reference values and contralateral hemisphere as internal control.

A 20-point neuroscore test was used to assess post-tMCAO motor and behavioral deficits at baseline, and on days 1, 3, 7, 14, 21, and 28 post-tMCAO. The neurological test was conducted and analyzed in a blinded manner. The following parameters were analyzed: Spontaneous circling (max. score 4), motility (max. score 3), general condition (max. score 3), paw placement on table top (max. score 4, 1 point per paw), righting reflex when placed on back (max. score 1), grip strength (max. score 2), contralateral reflex (max. score 1), visual forepaw reaching (max. score 2, 1 for each paw).

At the end-point (D30), the rats were transcardially perfused with heparinized (2.5 IU/ml) saline in order to remove blood from the brains and tissues. After perfusion with heparinized (2.5 IU/ml) saline, mice were perfused with 4% paraformaldehyde until fixed. Thereafter, whole brains were further immersion fixed in 4% paraformaldehyde in 0.1 M phosphate buffer (PB) for another 48 hr. Brains were then transferred to 0.1 M phosphate buffer (PB) and stored at 2–4 °C until analysis.

Immunohistochemistry was performed at NeuroScience Associates (Knoxville, TN, USA) as described above. The slides were digitally scanned by NeuroScience Associates using the TissueScope LE120 (Huron Digital Pathology, Ontario, Canada) slide scanner at a resolution of 0.40 micron/pixel. Quantitative image analysis was performed with the MatLab software package (MathWorks). Stained or immunolabeled areas were quantified in each hemisphere and normalized based on the total hemisphere tissue area. At least 27 serial sections were analyzed per stain per mouse and final scores were based on the average of those sections.

Statistical analysis

Data were analyzed using either GraphPad Prism or R. Statistical testing used for each analysis was listed in the corresponding figure legend. Data are represented by mean +/- SEM. Comparisons were considered statistically significant when $p < 0.05$.

Data and materials availability:

Sequencing data are available on GEO. Accessions numbers are: Single Cell RNAseq including P301S mice: GSE180041; Bulk RNAseq WT or TPL2-KD mice injected with PBS or LPS: GSE196401; Bulk RNAseq WT and TauP301S mouse hippocampus: GSE186414

Acknowledgements

We thank members of the Genentech animal care staff, fluorescence-activated cell sorting (FACS) laboratory, and CALM and RNA sequencing laboratory for research support. We thank Dwight Newton for uploading GSE196401 to GEO. We thank Chris Bohlen and Mark Wilson for critical reading of the manuscript.

Author contributions

Y.W., M.S and J.E.H. designed the project. Y.W., T.W., M.-C.T, L.X., K.S., M.S and J.E.H. designed and interpreted the experiments. Y.W., T.W., M.-C.T performed experiments and analyzed data. M.G.R., A.M.A., L.X., V.D.G., H.N., K.S., C.G., O.F., and B.A.F. analyzed the data. D.X. provided reagents. Y.W. and J.E.H wrote the manuscript. All authors read and edited the manuscript.

Declaration of interests

All authors are current or former employees of Genentech and Roche. The authors declare no competing financial interests.

References

Aran, D., Looney, A.P., Liu, L., Wu, E., Fong, V., Hsu, A., Chak, S., Naikawadi, R.P., Wolters, P.J., Abate, A.R., et al. (2019). Reference-based analysis of lung single-cell sequencing reveals a transitional profibrotic macrophage. Nat Immunol *20*, 163-172. 10.1038/s41590-018-0276-y.

Arthur, J.S., and Ley, S.C. (2013). Mitogen-activated protein kinases in innate immunity. Nat Rev Immunol *13*, 679-692. 10.1038/nri3495.

Bahrami, S., and Drablos, F. (2016). Gene regulation in the immediate-early response process. Adv Biol Regul *62*, 37-49. 10.1016/j.jbior.2016.05.001.

Bohlen, C.J., Friedman, B.A., Dejanovic, B., and Sheng, M. (2019). Microglia in Brain Development, Homeostasis, and Neurodegeneration. Annu Rev Genet *53*, 263-288. 10.1146/annurev-genet-112618-043515.

Brey, E.M., Lalani, Z., Johnston, C., Wong, M., McIntire, L.V., Duke, P.J., and Patrick, C.W., Jr. (2003). Automated selection of DAB-labeled tissue for immunohistochemical quantification. J Histochem Cytochem *51*, 575-584. 10.1177/002215540305100503.

Bright, F., Werry, E.L., Dobson-Stone, C., Piguet, O., Ittner, L.M., Halliday, G.M., Hodges, J.R., Kiernan, M.C., Loy, C.T., Kassiou, M., and Kril, J.J. (2019). Neuroinflammation in frontotemporal dementia. Nat Rev Neurol *15*, 540-555. 10.1038/s41582-019-0231-z.

Burman, M.A., Simmons, C.A., Hughes, M., and Lei, L. (2014). Developing and validating trace fear conditioning protocols in C57BL/6 mice. J Neurosci Methods *222*, 111-117. 10.1016/j.jneumeth.2013.11.005.

Cleveland, W.S., and McGill, R. (1985). Graphical perception and graphical methods for analyzing scientific data. Science *229*, 828-833. 10.1126/science.229.4716.828.

Dejanovic, B., Huntley, M.A., De Maziere, A., Meilandt, W.J., Wu, T., Srinivasan, K., Jiang, Z., Gandham, V., Friedman, B.A., Ngu, H., et al. (2018). Changes in the Synaptic Proteome in Tauopathy and Rescue of Tau-Induced Synapse Loss by C1q Antibodies. Neuron *100*, 1322-1336 e1327. 10.1016/j.neuron.2018.10.014.

Didonna, A. (2020). Tau at the interface between neurodegeneration and neuroinflammation. Genes Immun *21*, 288-300. 10.1038/s41435-020-00113-5.

Fassler, M., Rappaport, M.S., Cuno, C.B., and George, J. (2021). Engagement of TREM2 by a novel monoclonal antibody induces activation of microglia and improves cognitive function in Alzheimer's disease models. J Neuroinflammation *18*, 19. 10.1186/s12974-020-01980-5.

Friedman, B.A., Srinivasan, K., Ayalon, G., Meilandt, W.J., Lin, H., Huntley, M.A., Cao, Y., Lee, S.H., Haddick, P.C.G., Ngu, H., et al. (2018). Diverse Brain Myeloid Expression Profiles Reveal Distinct Microglial Activation States and Aspects of Alzheimer's Disease Not Evident in Mouse Models. Cell Rep *22*, 832-847. 10.1016/j.celrep.2017.12.066.

Gate, D., Saligrama, N., Leventhal, O., Yang, A.C., Unger, M.S., Middeldorp, J., Chen, K., Lehallier, B., Channappa, D., De Los Santos, M.B., et al. (2020). Clonally expanded CD8 T cells patrol the cerebrospinal fluid in Alzheimer's disease. Nature *577*, 399-404. 10.1038/s41586-019-1895-7.

Glass, C.K., Saijo, K., Winner, B., Marchetto, M.C., and Gage, F.H. (2010). Mechanisms underlying inflammation in neurodegeneration. Cell *140*, 918-934. 10.1016/j.cell.2010.02.016.

Han, C.J., O'Tuathaigh, C.M., van Trigt, L., Quinn, J.J., Fanselow, M.S., Mongeau, R., Koch, C., and Anderson, D.J. (2003). Trace but not delay fear conditioning requires attention and the anterior cingulate cortex. Proc Natl Acad Sci U S A *100*, 13087-13092. 10.1073/pnas.2132313100.

Hansen, D.V., Hanson, J.E., and Sheng, M. (2018). Microglia in Alzheimer's disease. J Cell Biol *217*, 459-472. 10.1083/jcb.201709069.

Heneka, M.T., Kummer, M.P., Stutz, A., Delekate, A., Schwartz, S., Vieira-Saecker, A., Griep, A., Axt, D., Remus, A., Tzeng, T.C., et al. (2013). NLRP3 is activated in Alzheimer's disease and contributes to pathology in APP/PS1 mice. Nature *493*, 674-678. 10.1038/nature11729.

Heng, T.S., Painter, M.W., and Immunological Genome Project, C. (2008). The Immunological Genome Project: networks of gene expression in immune cells. Nat Immunol *9*, 1091-1094. 10.1038/ni1008-1091.

Hong, S., Beja-Glasser, V.F., Nfonoyim, B.M., Frouin, A., Li, S., Ramakrishnan, S., Merry, K.M., Shi, Q., Rosenthal, A., Barres, B.A., et al. (2016). Complement and microglia mediate early synapse loss in Alzheimer mouse models. Science *352*, 712-716. 10.1126/science.aad8373.

Ising, C., Venegas, C., Zhang, S., Scheiblich, H., Schmidt, S.V., Vieira-Saecker, A., Schwartz, S., Albasset, S., McManus, R.M., Tejera, D., et al. (2019). NLRP3 inflammasome activation drives tau pathology. Nature *575*, 669-673. 10.1038/s41586-019-1769-z.

Laurent, C., Dorothee, G., Hunot, S., Martin, E., Monnet, Y., Duchamp, M., Dong, Y., Legeron, F.P., Leboucher, A., Burnouf, S., et al. (2017). Hippocampal T cell infiltration promotes neuroinflammation and cognitive decline in a mouse model of tauopathy. Brain *140*, 184-200. 10.1093/brain/aww270.

Law, C.W., Chen, Y., Shi, W., and Smyth, G.K. (2014). voom: Precision weights unlock linear model analysis tools for RNA-seq read counts. Genome Biol *15*, R29. 10.1186/gb-2014-15-2-r29.

Lee, S.H., Meilandt, W.J., Xie, L., Gandham, V.D., Ngu, H., Barck, K.H., Rezzonico, M.G., Imperio, J., Lalehzadeh, G., Huntley, M.A., et al. (2021a). Trem2 restrains the enhancement of tau accumulation and neurodegeneration by beta-amyloid pathology. Neuron *109*, 1283-1301 e1286. 10.1016/j.neuron.2021.02.010.

Lee, S.H., Rezzonico, M.G., Friedman, B.A., Huntley, M.H., Meilandt, W.J., Pandey, S., Chen, Y.J., Easton, A., Modrusan, Z., Hansen, D.V., et al. (2021b). TREM2-independent oligodendrocyte, astrocyte, and T cell responses to tau and amyloid pathology in mouse models of Alzheimer disease. Cell Rep *37*, 110158. 10.1016/j.celrep.2021.110158.

Leng, F., and Edison, P. (2021). Neuroinflammation and microglial activation in Alzheimer disease: where do we go from here? Nat Rev Neurol *17*, 157-172. 10.1038/s41582-020-00435-y.

Liddelow, S.A., Guttenplan, K.A., Clarke, L.E., Bennett, F.C., Bohlen, C.J., Schirmer, L., Bennett, M.L., Munch, A.E., Chung, W.S., Peterson, T.C., et al. (2017). Neurotoxic

reactive astrocytes are induced by activated microglia. Nature *541*, 481-487. 10.1038/nature21029.

Love, M.I., Huber, W., and Anders, S. (2014). Moderated estimation of fold change and dispersion for RNA-seq data with DESeq2. Genome Biol *15*, 550. 10.1186/s13059-014-0550-8.

Lun, A.T., McCarthy, D.J., and Marioni, J.C. (2016). A step-by-step workflow for low-level analysis of single-cell RNA-seq data with Bioconductor. F1000Res *5*, 2122. 10.12688/f1000research.9501.2.

Maphis, N., Xu, G., Kokiko-Cochran, O.N., Jiang, S., Cardona, A., Ransohoff, R.M., Lamb, B.T., and Bhaskar, K. (2015). Reactive microglia drive tau pathology and contribute to the spreading of pathological tau in the brain. Brain *138*, 1738-1755. 10.1093/brain/awv081.

Merlini, M., Kirabali, T., Kulic, L., Nitsch, R.M., and Ferretti, M.T. (2018). Extravascular CD3+ T Cells in Brains of Alzheimer Disease Patients Correlate with Tau but Not with Amyloid Pathology: An Immunohistochemical Study. Neurodegener Dis *18*, 49-56. 10.1159/000486200.

Ndoja, A., Reja, R., Lee, S.H., Webster, J.D., Ngu, H., Rose, C.M., Kirkpatrick, D.S., Modrusan, Z., Chen, Y.J., Dugger, D.L., et al. (2020). Ubiquitin Ligase COP1 Suppresses Neuroinflammation by Degrading c/EBPbeta in Microglia. Cell *182*, 1156-1169 e1112. 10.1016/j.cell.2020.07.011.

Neefjes, J., Jongsma, M.L., Paul, P., and Bakke, O. (2011). Towards a systems understanding of MHC class I and MHC class II antigen presentation. Nat Rev Immunol *11*, 823-836. 10.1038/nri3084.

O'Donnell, A., Odrowaz, Z., and Sharrocks, A.D. (2012). Immediate-early gene activation by the MAPK pathways: what do and don't we know? Biochem Soc Trans *40*, 58-66. 10.1042/BST20110636.

Odagiu, L., May, J., Boulet, S., Baldwin, T.A., and Labrecque, N. (2020). Role of the Orphan Nuclear Receptor NR4A Family in T-Cell Biology. Front Endocrinol (Lausanne) *11*, 624122. 10.3389/fendo.2020.624122.

Papageorgiou, I.E., Lewen, A., Galow, L.V., Cesetti, T., Scheffel, J., Regen, T., Hanisch, U.K., and Kann, O. (2016). TLR4-activated microglia require IFN-gamma to induce severe neuronal dysfunction and death in situ. Proc Natl Acad Sci U S A *113*, 212-217. 10.1073/pnas.1513853113.

Roche, P.A., and Furuta, K. (2015). The ins and outs of MHC class II-mediated antigen processing and presentation. Nat Rev Immunol *15*, 203-216. 10.1038/nri3818.

Senger, K., Pham, V.C., Varfolomeev, E., Hackney, J.A., Corzo, C.A., Collier, J., Lau, V.W.C., Huang, Z., Hamidzhadeh, K., Caplazi, P., et al. (2017). The kinase TPL2 activates ERK and p38 signaling to promote neutrophilic inflammation. Sci Signal *10*. 10.1126/scisignal.aah4273.

Sharma, V., Cohen, N., Sood, R., Ounallah-Saad, H., Gal-Ben-Ari, S., and Rosenblum, K. (2018). Trace Fear Conditioning: Procedure for Assessing Complex Hippocampal Function in Mice. Bio Protoc *8*, e2475. 10.21769/BioProtoc.2475.

Sheng, W., Zong, Y., Mohammad, A., Ajit, D., Cui, J., Han, D., Hamilton, J.L., Simonyi, A., Sun, A.Y., Gu, Z., et al. (2011). Pro-inflammatory cytokines and lipopolysaccharide induce changes in cell morphology, and upregulation of ERK1/2, iNOS and sPLA(2)-

908 IIA expression in astrocytes and microglia. J Neuroinflammation *8*, 121.
909 10.1186/1742-2094-8-121.
910 Srinivasan, K., Friedman, B.A., Etxeberria, A., Huntley, M.A., van der Brug, M.P.,
911 Foreman, O., Paw, J.S., Modrusan, Z., Beach, T.G., Serrano, G.E., and Hansen, D.V.
912 (2020). Alzheimer's Patient Microglia Exhibit Enhanced Aging and Unique
913 Transcriptional Activation. Cell Rep *31*, 107843. 10.1016/j.celrep.2020.107843.
914 Srinivasan, K., Friedman, B.A., Larson, J.L., Lauffer, B.E., Goldstein, L.D., Appling, L.L.,
915 Borneo, J., Poon, C., Ho, T., Cai, F., et al. (2016). Untangling the brain's
916 neuroinflammatory and neurodegenerative transcriptional responses. Nat Commun
917 *7*, 11295. 10.1038/ncomms11295.
918 Sriskantharajah, S., Guckel, E., Tsakiri, N., Kierdorf, K., Brender, C., Ben-Addi, A.,
919 Veldhoen, M., Tsichlis, P.N., Stockinger, B., O'Garra, A., et al. (2014). Regulation of
920 experimental autoimmune encephalomyelitis by TPL-2 kinase. J Immunol *192*,
921 3518-3529. 10.4049/jimmunol.1300172.
922 Stark, K., Goncharov, T., Varfolomeev, E., Xie, L., Ngu, H., Peng, I., Anderson, K.R.,
923 Verschueren, E., Choi, M., Kirkpatrick, D.S., et al. (2021). Genetic inactivation of RIP1
924 kinase activity in rats protects against ischemic brain injury. Cell Death Dis *12*, 379.
925 10.1038/s41419-021-03651-6.
926 Stephan, A.H., Barres, B.A., and Stevens, B. (2012). The complement system: an
927 unexpected role in synaptic pruning during development and disease. Annu Rev
928 Neurosci *35*, 369-389. 10.1146/annurev-neuro-061010-113810.
929 Straccia, M., Gresa-Arribas, N., Dentesano, G., Ejarque-Ortiz, A., Tusell, J.M., Serratosa,
930 J., Sola, C., and Saura, J. (2011). Pro-inflammatory gene expression and neurotoxic
931 effects of activated microglia are attenuated by absence of CCAAT/enhancer binding
932 protein beta. J Neuroinflammation *8*, 156. 10.1186/1742-2094-8-156.
933 Stuart, T., Butler, A., Hoffman, P., Hafemeister, C., Papalexi, E., Mauck, W.M., 3rd, Hao,
934 Y., Stoeckius, M., Smibert, P., and Satija, R. (2019). Comprehensive Integration of
935 Single-Cell Data. Cell *177*, 1888-1902 e1821. 10.1016/j.cell.2019.05.031.
936 Togo, T., Akiyama, H., Iseki, E., Kondo, H., Ikeda, K., Kato, M., Oda, T., Tsuchiya, K., and
937 Kosaka, K. (2002). Occurrence of T cells in the brain of Alzheimer's disease and
938 other neurological diseases. J Neuroimmunol *124*, 83-92. 10.1016/s0165-
939 5728(01)00496-9.
940 Wang, S., Mustafa, M., Yuede, C.M., Salazar, S.V., Kong, P., Long, H., Ward, M., Siddiqui,
941 O., Paul, R., Gilfillan, S., et al. (2020). Anti-human TREM2 induces microglia
942 proliferation and reduces pathology in an Alzheimer's disease model. J Exp Med *217*.
943 10.1084/jem.20200785.
944 Wang, W.Y., Tan, M.S., Yu, J.T., and Tan, L. (2015). Role of pro-inflammatory
945 cytokines released from microglia in Alzheimer's disease. Ann Transl Med *3*, 136.
946 10.3978/j.issn.2305-5839.2015.03.49.
947 Watkins, T.A., Wang, B., Huntwork-Rodriguez, S., Yang, J., Jiang, Z., Eastham-
948 Anderson, J., Modrusan, Z., Kaminker, J.S., Tessier-Lavigne, M., and Lewcock, J.W.
949 (2013). DLK initiates a transcriptional program that couples apoptotic and
950 regenerative responses to axonal injury. Proc Natl Acad Sci U S A *110*, 4039-4044.
951 10.1073/pnas.1211074110.

952 Webb, L.V., Ventura, S., and Ley, S.C. (2019). ABIN-2, of the TPL-2 Signaling Complex,
953 Modulates Mammalian Inflammation. Trends Immunol *40*, 799-808.
954 10.1016/j.it.2019.07.001.
955 Wherry, E.J. (2011). T cell exhaustion. Nat Immunol *12*, 492-499. 10.1038/ni.2035.
956 Wherry, E.J., and Kurachi, M. (2015). Molecular and cellular insights into T cell
957 exhaustion. Nat Rev Immunol *15*, 486-499. 10.1038/nri3862.
958 Wilton, D.K., Dissing-Olesen, L., and Stevens, B. (2019). Neuron-Glia Signaling in
959 Synapse Elimination. Annu Rev Neurosci *42*, 107-127. 10.1146/annurev-neuro-
960 070918-050306.
961 Wu, T., Dejanovic, B., Gandham, V.D., Gogineni, A., Edmonds, R., Schauer, S.,
962 Srinivasan, K., Huntley, M.A., Wang, Y., Wang, T.M., et al. (2019). Complement C3 Is
963 Activated in Human AD Brain and Is Required for Neurodegeneration in Mouse
964 Models of Amyloidosis and Tauopathy. Cell Rep *28*, 2111-2123 e2116.
965 10.1016/j.celrep.2019.07.060.
966 Wu, T.D., and Nacu, S. (2010). Fast and SNP-tolerant detection of complex variants
967 and splicing in short reads. Bioinformatics *26*, 873-881.
968 10.1093/bioinformatics/btq057.
969 Xiao, Y., Jin, J., Chang, M., Nakaya, M., Hu, H., Zou, Q., Zhou, X., Brittain, G.C., Cheng, X.,
970 and Sun, S.C. (2014). TPL2 mediates autoimmune inflammation through activation
971 of the TAK1 axis of IL-17 signaling. J Exp Med *211*, 1689-1702.
972 10.1084/jem.20132640.
973 Xu, D., Matsumoto, M.L., McKenzie, B.S., and Zarrin, A.A. (2018). TPL2 kinase action
974 and control of inflammation. Pharmacol Res *129*, 188-193.
975 10.1016/j.phrs.2017.11.031.
976 Yartseva, V., Goldstein, L.D., Rodman, J., Kates, L., Chen, M.Z., Chen, Y.J., Foreman, O.,
977 Siebel, C.W., Modrusan, Z., Peterson, A.S., and Jovicic, A. (2020). Heterogeneity of
978 Satellite Cells Implicates DELTA1/NOTCH2 Signaling in Self-Renewal. Cell Rep *30*,
979 1491-1503 e1496. 10.1016/j.celrep.2019.12.100.
980 Yeh, F.L., Wang, Y., Tom, I., Gonzalez, L.C., and Sheng, M. (2016). TREM2 Binds to
981 Apolipoproteins, Including APOE and CLU/APOJ, and Thereby Facilitates Uptake of
982 Amyloid-Beta by Microglia. Neuron *91*, 328-340. 10.1016/j.neuron.2016.06.015.
983 Yi, J.S., Cox, M.A., and Zajac, A.J. (2010). T-cell exhaustion: characteristics, causes and
984 conversion. Immunology *129*, 474-481. 10.1111/j.1365-2567.2010.03255.x.
985 Yoshiyama, Y., Higuchi, M., Zhang, B., Huang, S.M., Iwata, N., Saido, T.C., Maeda, J.,
986 Suhara, T., Trojanowski, J.Q., and Lee, V.M. (2007). Synapse loss and microglial
987 activation precede tangles in a P301S tauopathy mouse model. Neuron *53*, 337-351.
988 10.1016/j.neuron.2007.01.010.
989 Zarrin, A.A., Bao, K., Lupardus, P., and Vucic, D. (2021). Kinase inhibition in
990 autoimmunity and inflammation. Nat Rev Drug Discov *20*, 39-63. 10.1038/s41573-
991 020-0082-8.
992 Zeisel, A., Hochgerner, H., Lonnerberg, P., Johnsson, A., Memic, F., van der Zwan, J.,
993 Haring, M., Braun, E., Borm, L.E., La Manno, G., et al. (2018). Molecular Architecture
994 of the Mouse Nervous System. Cell *174*, 999-1014 e1022.
995 10.1016/j.cell.2018.06.021.
996 Zhang, Y., Chen, K., Sloan, S.A., Bennett, M.L., Scholze, A.R., O'Keeffe, S., Phatnani, H.P.,
997 Guarnieri, P., Caneda, C., Ruderisch, N., et al. (2014). An RNA-sequencing

transcriptome and splicing database of glia, neurons, and vascular cells of the cerebral cortex. J Neurosci *34*, 11929-11947. 10.1523/JNEUROSCI.1860-14.2014.

Zhou, M., Xu, R., Kaelber, D.C., and Gurney, M.E. (2020). Tumor Necrosis Factor (TNF) blocking agents are associated with lower risk for Alzheimer's disease in patients with rheumatoid arthritis and psoriasis. PLoS One *15*, e0229819. 10.1371/journal.pone.0229819.

Fig. 1

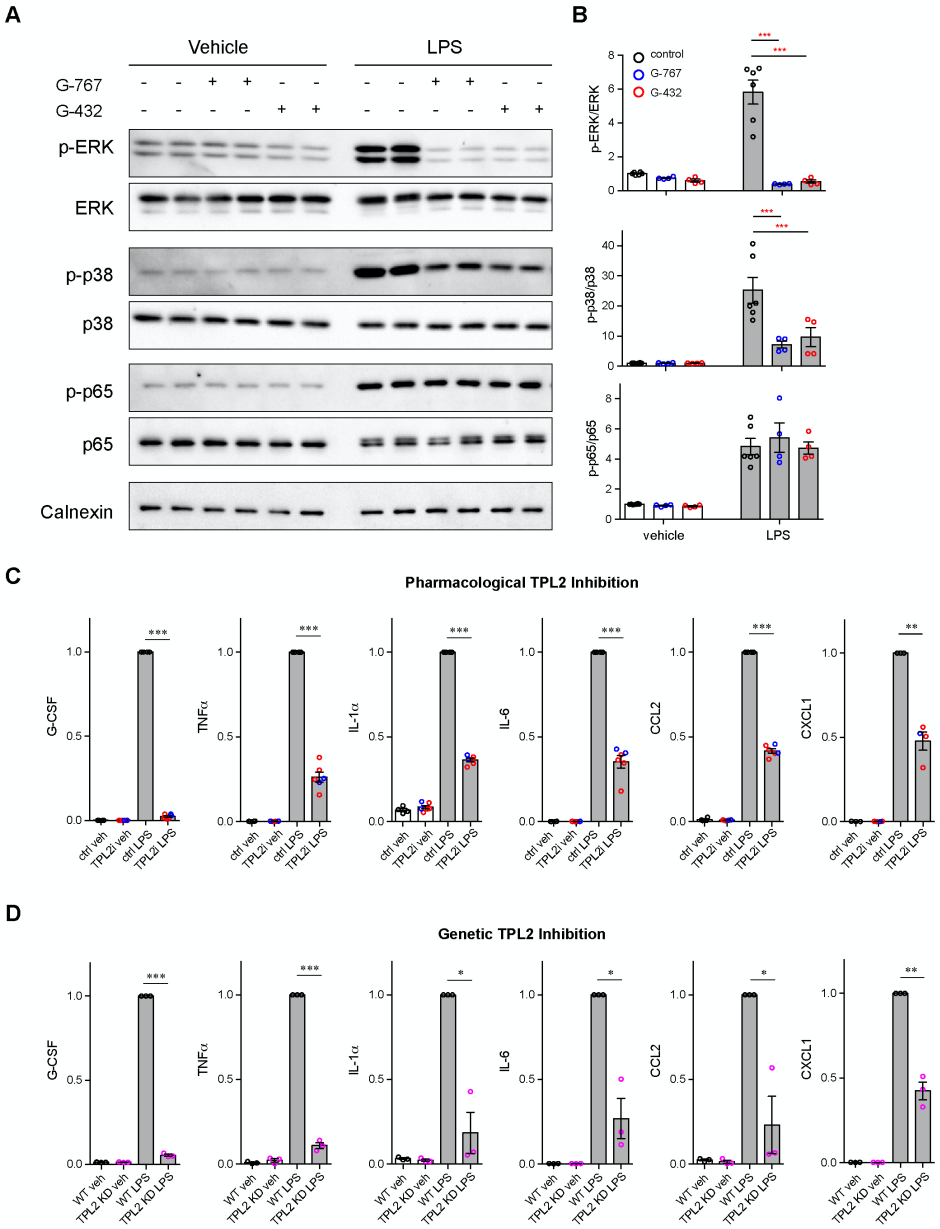

Fig. 1. TPL2 modulates MAPK signaling and cytokine production by microglia.

A, Representative western blots of phospho-ERK, total ERK, phospho-p38, total p38, phospho-p65, total p65 and Calnexin (loading control) in lysates from primary microglia cultures treated with vehicle or LPS with or without TPL2 inhibitors (2 μM). **B**, Quantification of western blot data as shown in (**A**). Phosphorylated proteins were first normalized to the corresponding total proteins, and then the normalized values were plotted relative to the average values from control samples (no LPS, no TPL2 inhibitor) n = 4-6. Data are represented by mean +/- SEM. ***, $p < 0.001$, two-way ANOVA with Tukey's multiple comparisons test. **C** and **D**, Quantification of cytokine measurements from the supernatants of WT primary microglia with or without TPL2 inhibitor (**C**) or microglia isolated from WT mice or TPL2KD mice (**D**) under control or LPS induction (24 hr incubation) conditions. Cytokines highlighted here were selected based on significant LPS induction that was reduced by TPL2 inhibition (pharmacological or genetic) by > 50%. Additional cytokine measurements are provided in Fig. S2. Cytokine measurements were normalized to average values of WT microglia treated with LPS. Data from TPL2 inhibitor G-432 (red circle) and G-767 (blue circle) were combined in (c), n = 4-6. n = 3 for (d). Data are represented by mean +/- SEM. *, $p < 0.05$, **, $p < 0.01$, ***, $p < 0.001$, one-way ANOVA with Tukey's multiple comparisons test.

Fig.1-source data: full images of Fig. 1A western blots are available.

Fig. 2

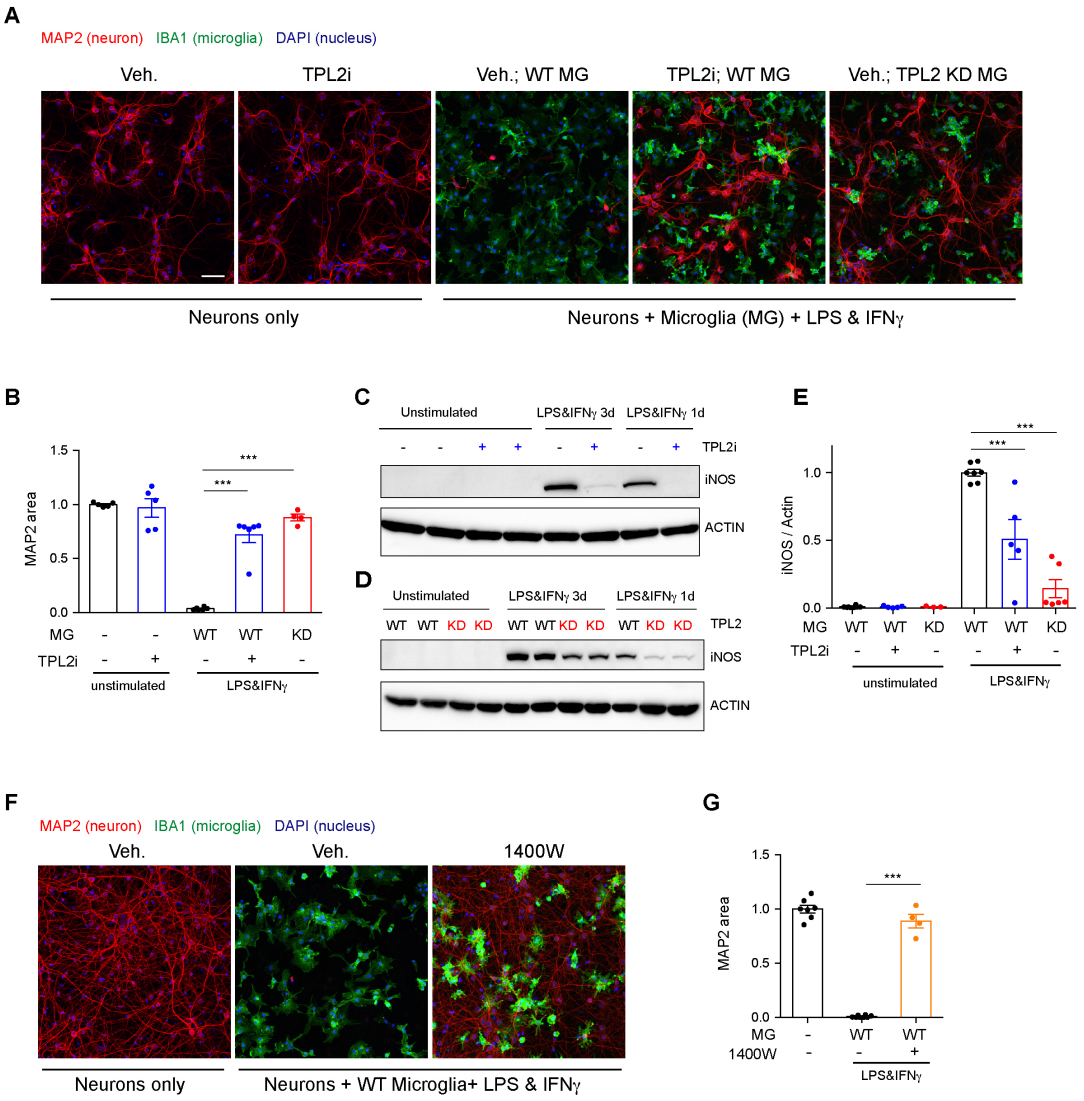

Fig. 2. TPL2 inhibition rescues neurodegeneration in a co-culture model.

A, Representative images of immunostaining for MAP2 (red), IBA1 (green) and DAPI (blue) in mouse cortical neuronal cultures or mouse cortical neurons co-cultured with mouse microglia as indicated. Cell number ratio in co-cultures is 1:1. Neurons were always cultured from WT mice and microglia were either from WT mice or TPL2KD mice as indicated. **B**, Quantification of MAP2 staining positive area within the image field as a readout of surviving neurons in the culture. MAP2 area is shown as normalized relative to the average value of the control condition (no microglia, no stimulation). n = 5-6 per condition. **C** and **D**, Representative immunoblots of iNOS (inducible nitric oxide synthase) from primary microglia cultures with treatments as indicated. Comparison was done either between WT microglia treated with and without TPL2 inhibitor (**C**), or between microglia isolated from WT mice and TPL2KD mice (**D**). **e**, Quantification of western blot data in (**D**) and (**D**). iNOS signal was normalized to actin signal, and the normalized values were plotted relative to the average value of the lysates from WT microglia treated with LPS and interferon gamma. n = 3-8. **F**, Representative images of immunostaining of MAP2 (red), IBA1 (green) and DAPI (blue) in mouse cortical neuronal cultures or mouse cortical neurons co-cultured with mouse microglia as indicated. Cell number ratio in co-cultures is 1:1. **G**, Quantification of MAP2 staining is shown as in (**B**). n = 4-8. For all bar graphs, data are represented by mean +/- SEM. ***, $p < 0.001$, one-way ANOVA with Tukey's multiple comparisons test.

Fig.2-source data: full images of Fig. 2C and 2D western blots are available.

Fig. 3

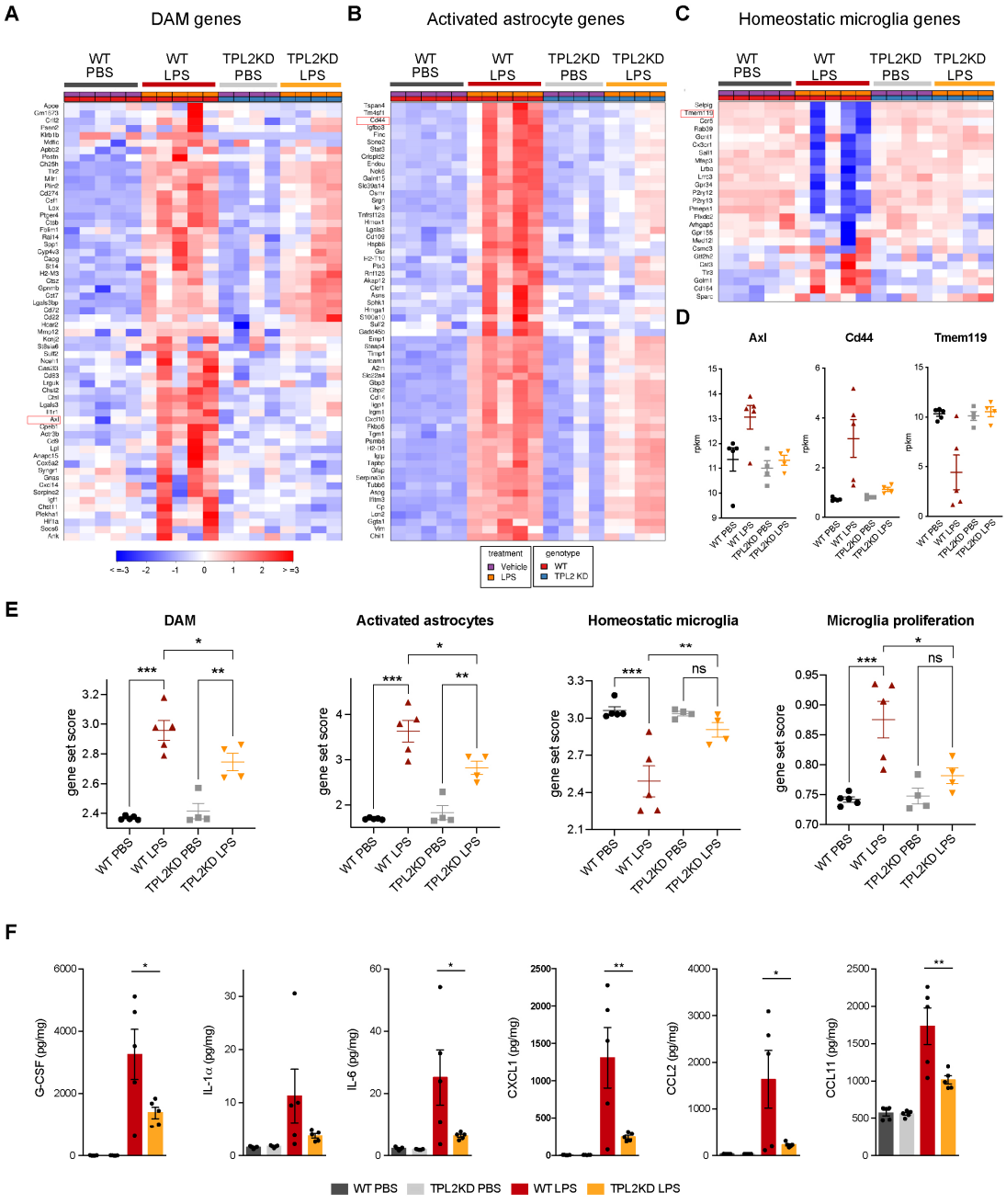

Fig. 3. TPL2KD mice have attenuated gene expression changes and cytokine/chemokine response after LPS injection.

A, Heatmap showing z scores of the top 60 DAM genes (disease associated microglia genes) in the brains of WT or TPL2KD mice injected with PBS or LPS. The top 60 DAM genes were taken from the list in(Friedman *et al*., 2018), and were selected based on the ranking of z scores of these genes in WT mice injected with LPS. **B**, Heatmap showing z scores of the top 60 activated astrocyte genes taken from the list in(Wu *et al*., 2019) (both A1 and A2 astrocyte genes were included). The top 60 genes were also selected based on the ranking of z-scores of these genes in WT mice injected with LPS. **C**, Heatmap showing z-scores of homeostatic microglia genes from(Friedman *et al*., 2018). **D**, Examples of DAM genes (*Axl*), astrocyte activated genes (*Cd44*) and homeostatic microglia genes (*Tmem119*). **E**, Geneset score expression of DAM genes, activated astrocyte genes, homeostatic microglia genes and microglia proliferation genes in mouse brain samples with different treatments as indicated. n = 4-5 animals per condition. **F**, Cytokine and chemokine levels in mouse brain lysates from the same mice as in (**A** - **E**) measured using a bead-based multiplex assay. Cytokine levels were normalized to total protein concentration in brain lysates and are shown as pg/mg. Only analytes that were above the detection level, changed after LPS injection, and exhibited a difference between WT and TPL2KD mice are shown. Data are represented by mean +/- SEM. *, $p < 0.05$, **, $p < 0.01$, ***, $p < 0.001$, one-way ANOVA with Tukey's multiple comparisons test.

Fig. 4

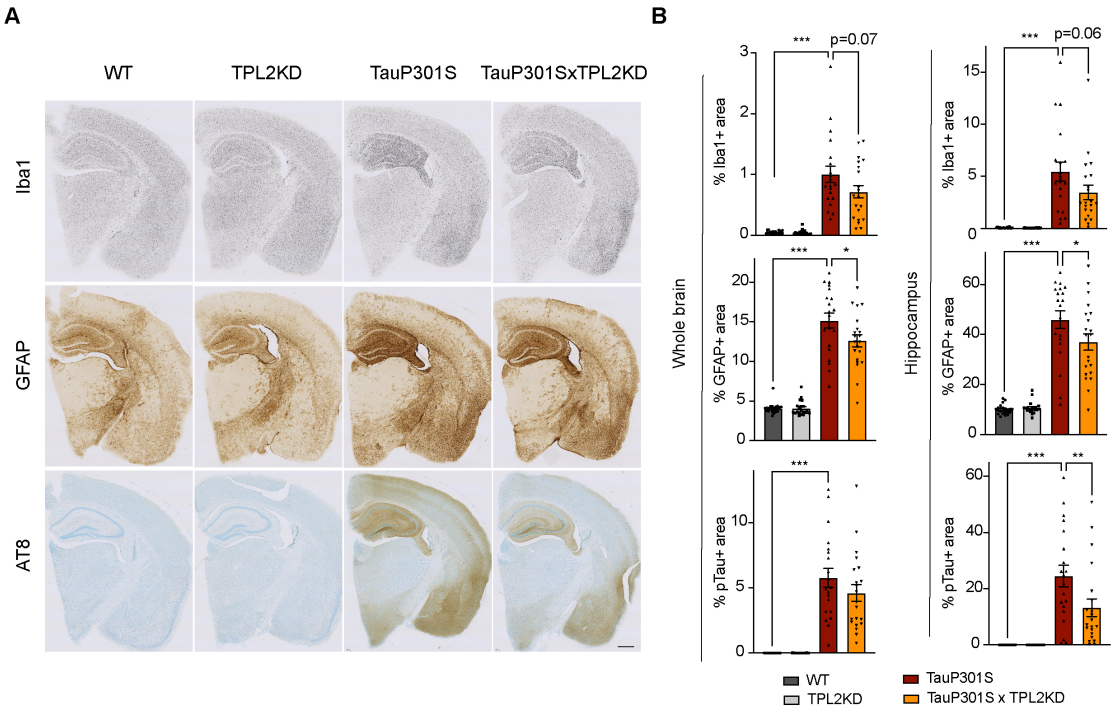

Fig. 4. TPL2KD partially rescues neuroinflammation in TauP301S mouse brain.

A, Representative images showing immunostaining for Iba1, GFAP and AT8 in mouse hemibrains from 9-month-old male mice with genotypes as indicated. Scale bar, 500 μm. **B**, Quantification of percentage of Iba1, GFAP, AT8 positive area within mouse hemibrains and specifically within the hippocampus as indicated. Analysis shown are combined data from 9-month-old male mice and 11-month-old female mice. Each dot represents one animal. **C**, A subset of cytokines or chemokine levels in mouse hippocampal lysates measured using bead-based mouse cytokine multiplex assay. Cytokine levels were normalized to total protein concentration in brain lysates and are shown as pg/mg. Data shown include protein levels from both 9-month-old male mice and 11-month-old female mice. For all bar graphs, data are represented by mean +/- SEM. *, $p < 0.05$, ***, $p < 0.001$, one-way ANOVA with Tukey's multiple comparisons test.

Fig. 5

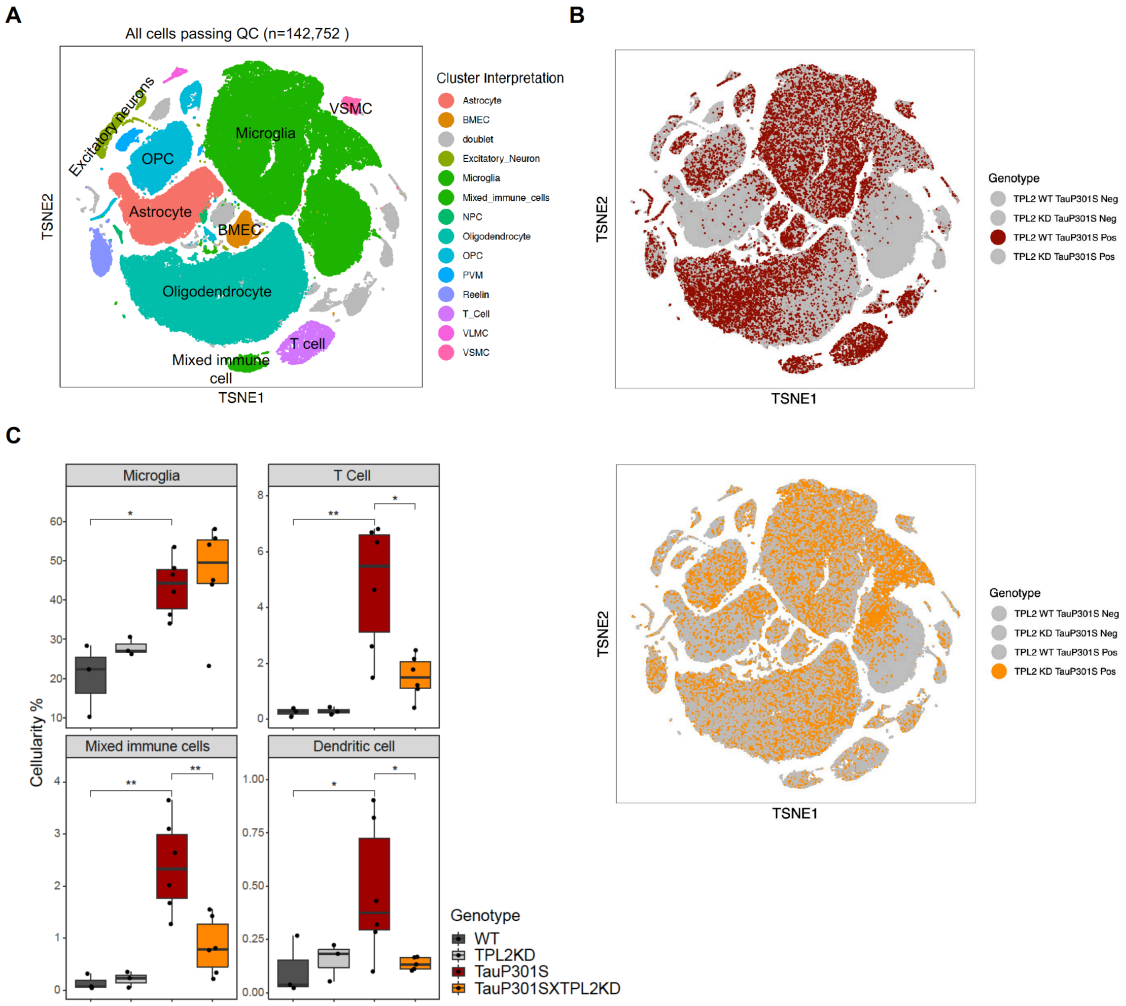

Fig. 5. Single-cell RNA-seq shows TPL2KD normalizes increased T cells and dendritic cells in TauP301S brains.

A, tSNE dimensional reduction and cell type interpretation of 142,752 hippocampal cells from 9-month-old TPL2 WT/KD TauP301S positive/negative mice. **B**, Distribution of cells by TPL2 genotype in TauP301S Positive samples. **C**, "Cellularity plot" illustrating proportions of microglia, mixed immune cells, T cells, and dendritic cells (as identified from further analysis of the mixed immune cell cluster described in supplementary Fig. S8) in each genotype. Each point represents a single animal, and the y-axis is the percentage of all cells in the scRNA-Seq dataset for that animal of the given cell type. Boxplots showing summarized distribution of the percentage; P values are based on t-test between indicated groups using ggpubr. *, $p < 0.05$, **, $p < 0.01$.

Fig. 6

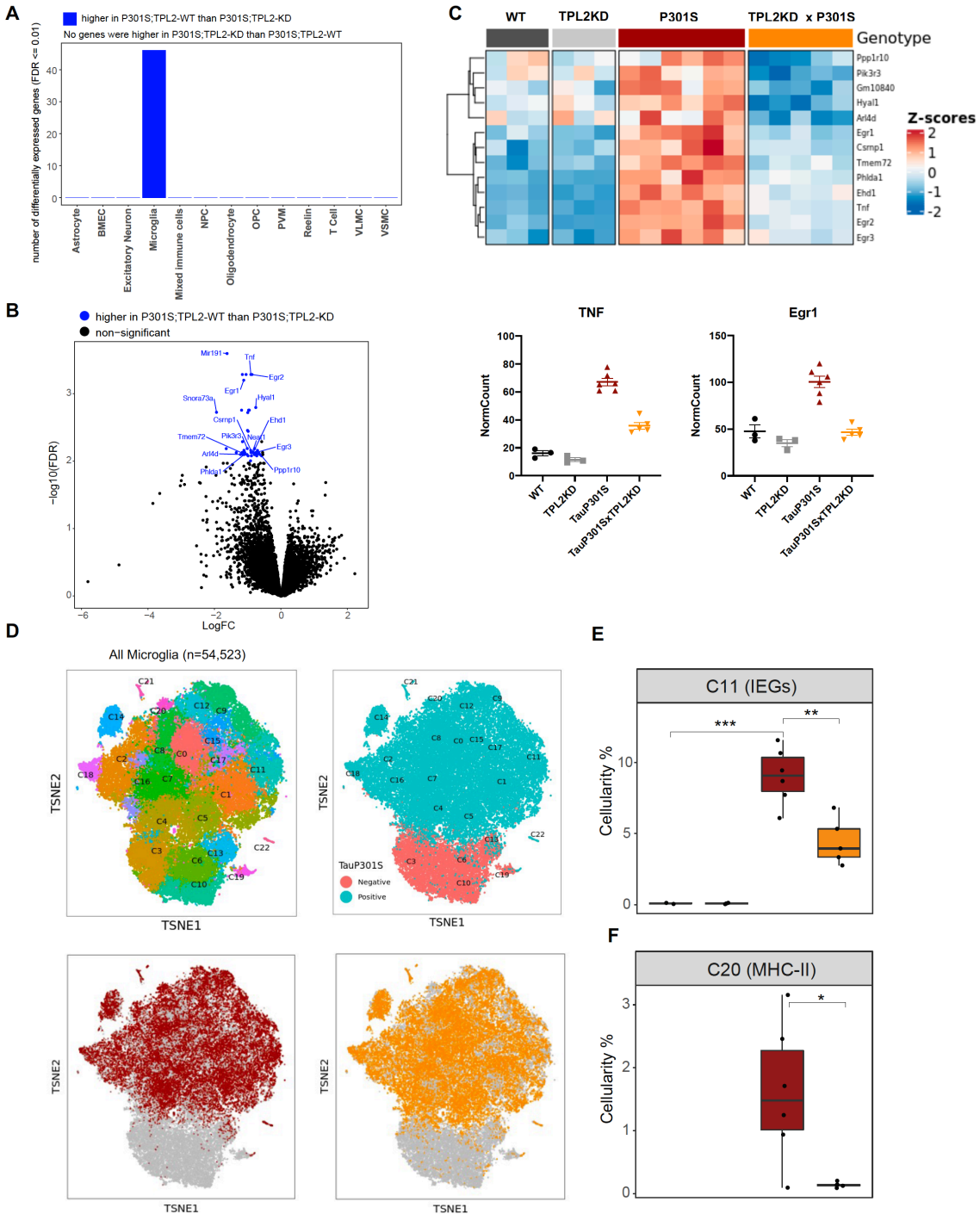

Fig. 6. TPL2KD partially normalizes elevated gene expression in TauP301S microglia and reduces the abundance of microglia in specific P301S-induced clusters.

A, Number of significantly differentially expressed genes (DEGs) for each cell type from pseudobulk analysis at FDR < 0.01 and Log2(fold-change) > 1.5 or < -1.5 between P301S and P301S;TPL2KD genotypes. **B**, Volcano plot showing differentially expressed genes for microglia from pseudobulk analysis between P301S and P301S;TPL2KD genotypes. Only protein-coding genes were annotated. **C**, Heatmap showing z-scores of Log2(normCount+1) for microglia DEGs as shown in (**B**). Boxplots summarizing expression levels of selected genes from the heatmap using normalized counts across the 4 genotypes used in this study. **D**, tSNE-based subclustering of n = 54,523 microglia defined from Fig. 5A, colored by subcluster identity and genotypes. **E** and **F**, Cellularity plot, similar to Fig. 5C, showing for each sample the percentage of microglia in subclusters C11 or C20 as a percentage of the total number of microglia cells in that sample. P values are based on t-test between indicated groups. *, $p < 0.05$, **, $p < 0.01$.

Fig. 7

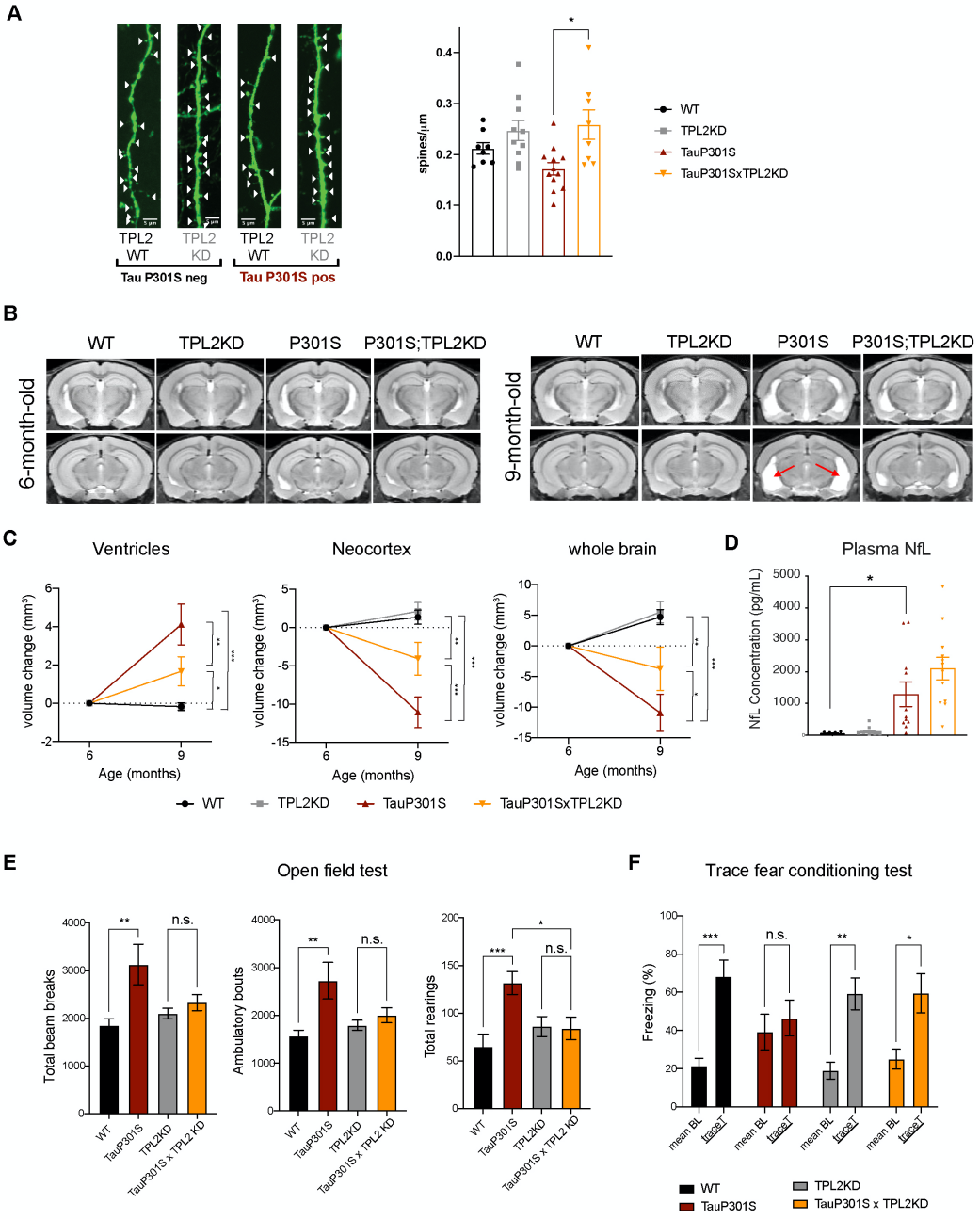

Fig. 7. TPL2 functional deficiency attenuates brain atrophy and recues behavioral deficits in TauP301S mice

A, Ex vivo imaging of fixed mouse hemibrains of 9-month-old male mice. Representative confocal z-stack images of GFP-expressing neurons are shown on the left with genotypes as indicated. White arrow heads point to the dendritic spines. Scale bar, 5 μm. Right, quantification of spine density as shown on the left. Each dot represents one mouse (average of 6 dendrites). n = 8-12. Data are represented by mean +/- SEM. *, $p < 0.05$, one-way ANOVA with Tukey's multiple comparisons test. **B**, Representative volumetric MRI images in 6-month-old and 9-month-old male mice with genotypes as indicated. Arrow indicates enlargement of ventricles at 9 months of age compared with 6 months in P301S mice. **C**, Longitudinal volumetric MRI quantification shows volume changes of ventricles, neocortex and whole brain at 9 months of age compared with 6 months of age. Comparisons between all four genotypes at 9 months of age showed significant increase of ventricle volumes and decrease of neocortex and whole brain volumes in TauP301S mice and TPLKD showed partial rescue of the TauP301S dependent volume changes. n = 11-12 male mice per genotype. Data are represented by mean +/- SEM. *, $p < 0.05$, **, $p < 0.01$, ***, $p < 0.001$, two-way ANOVA with Tukey's multiple comparisons test. **D**, Quantification of plasma NfL levels from mice in (**c**). **E**, Spontaneous locomotor activity of mice were evaluated in open field tests including total beam breaks, ambulatory bouts and total rearings during a 20 min period. TauP301S mice showed hyperactivity, which was rescued by TPL2KD. n = 22-24 animals per genotype with male and female mice combined. *, $p < 0.05$, **, $p < 0.01$, ***, $p < 0.001$, one-way ANOVA with Tukey's multiple comparisons test. **F**, Memory of mice was evaluated using trace fear conditioning test. Percentage of time freezing during baseline recording time and during the trace interval time after the conditioned stimulus tone was compared for each genotype. n =10-12 animals per genotype. Data are represented by mean +/- SEM. *, $p < 0.05$, **, $p < 0.01$, ***, $p < 0.001$, two-way ANOVA with Bonferroni's multiple comparisons test.

Supplementary Figures (S1-S12)

Fig. S1

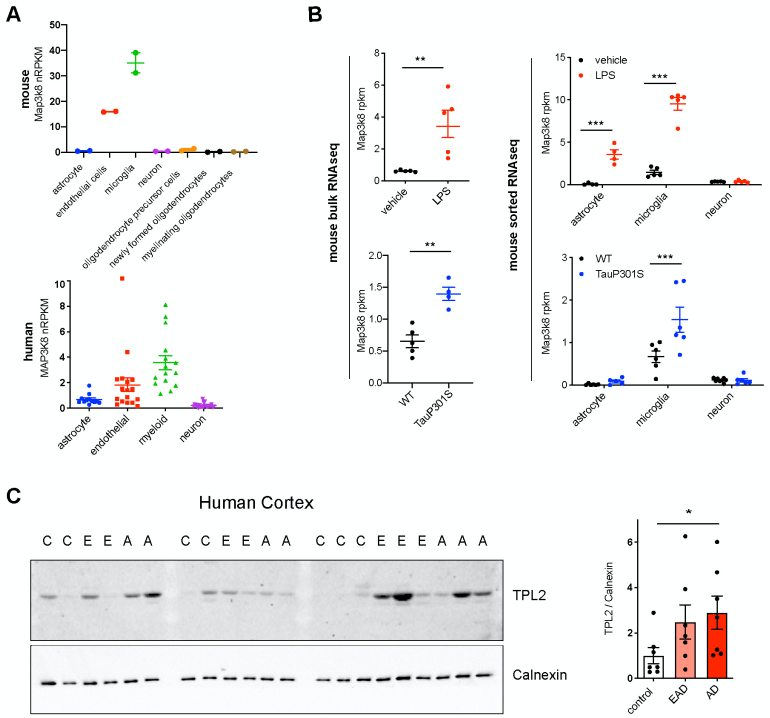

Fig. S1. TPL2 is upregulated in Tauopathy mice and AD patients.

A, Expression of TPL2 (Map3k8) in various cell types, as indicated, sorted from mouse brain tissue (Zhang *et al*., 2014) (top) or human brain tissue (Srinivasan *et al*., 2020) (bottom). **B**, Expression of TPL2 in brain bulk tissue (top left; GSE196401) or sorted astrocytes, microglia and neurons (top right (Srinivasan *et al*., 2016)) from WT mice injected with PBS or LPS (10 mg/kg). n = 4-5. Expression of TPL2 was also examined in hippocampal bulk tissue (bottom left; GSE186414) or sorted astrocytes, microglia and neurons (bottom right (Friedman *et al*., 2018)) from hippocampi of WT and TauP301S mice. **C**, Western blot image and quantification of TPL2 and calnexin as a loading control in lysates from human superior frontal gyrus of healthy control (C), early AD (E or EAD) and AD (A or AD) patient brains. TPL2 protein levels were normalized to the average control level after normalization to Calnexin. Data are represented by mean +/- SEM. *, $p < 0.05$, two-tailed Student's t-test.

Supplementary Fig.S1-source data: full images of Fig. S1C western blots are available.

1239 Fig. S2

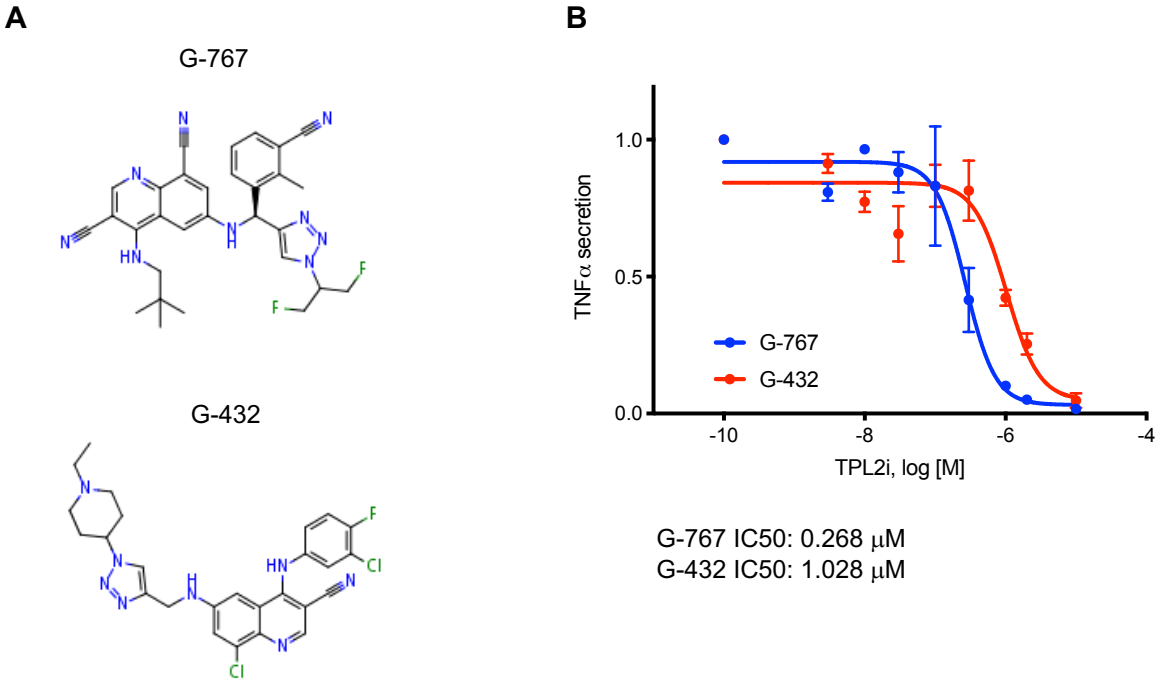

1240

1241

1242 **Fig. S2. TPL2 inhibitor structures and potency dose response curves.**

1243 **A,** Structures of TPL2 inhibitors G-432 and G-767. **B**, Inhibition dose response curve of TPL2

1244 inhibitor G-432 or G-767. Measurements were done with primary microglia cultures stimulated

1245 with LPS, using TNFα levels in the cell culture supernatants as the readout. TNFα levels were

1246 normalized to average values of microglia treated with LPS, without inhibitor.

1247

1248

1249

1250

1251

1252

Fig. S3

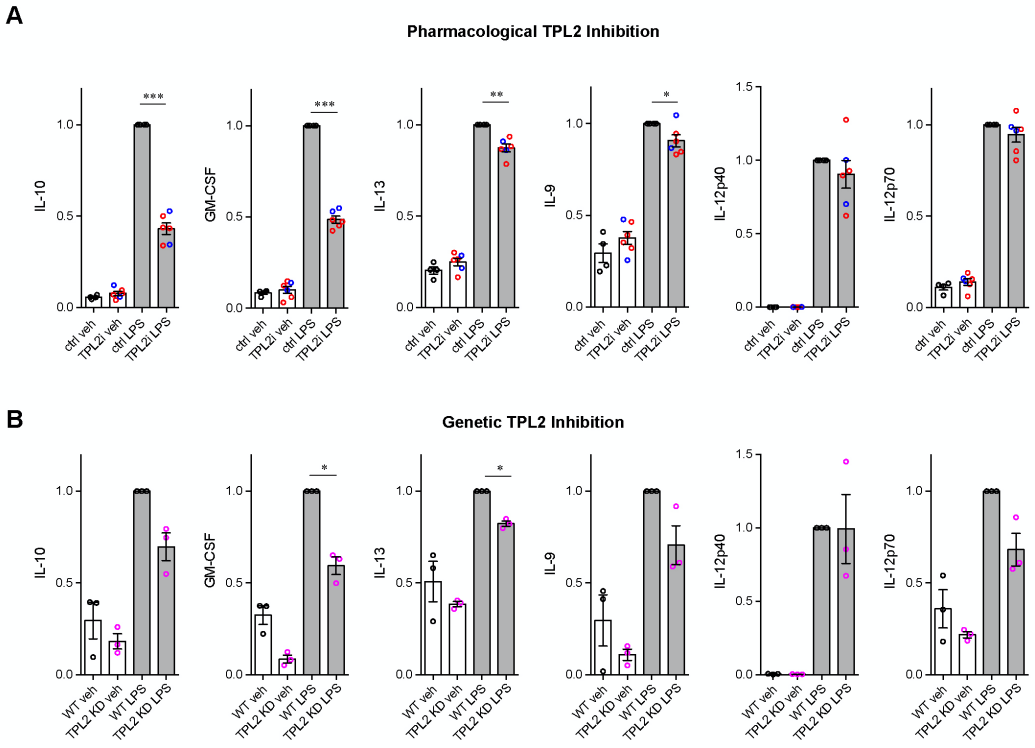

Fig. S3. Cytokine and chemokine release by microglia after LPS stimulation. Related to Fig. 1.

Additional cytokine and chemokine measurements from the same samples as shown in Fig. 1C,D are shown here. Cytokine and chemokine levels from the supernatants of WT primary microglia with or without TPL2 inhibitor (**A**) or microglia isolated from WT mice or TPL2KD mice (**B**) under control or LPS induction (24 hr incubation) conditions as indicated. Data are represented by mean +/- SEM. *, $p < 0.05$, **, $p < 0.01$, ***, $p < 0.001$, one-way ANOVA with Tukey's multiple comparisons test.

Fig. S4

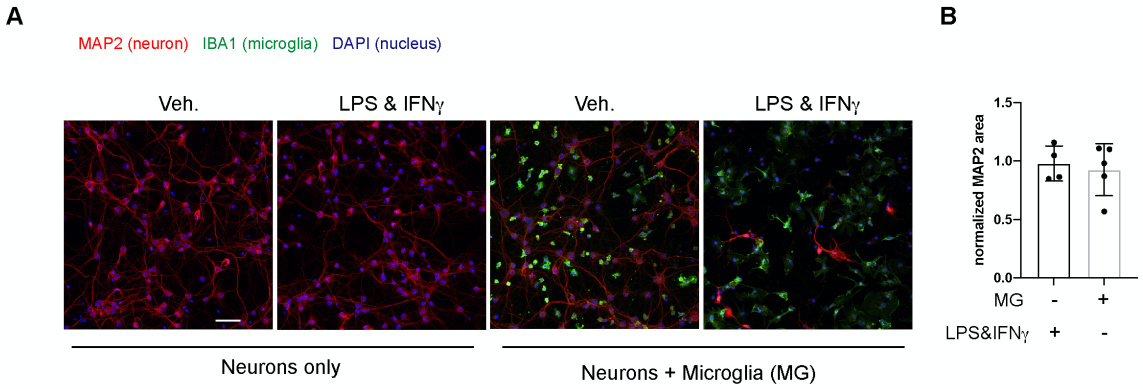

Fig. S4. Stimulation of neurons cultured without microglia or co-culture of neurons and microglia without stimulation does not result in neuronal loss.

A, Representative images of immunostaining of MAP2 (red), IBA1 (green) and DAPI (blue) in mouse cortical neuronal cultures or mouse cortical neurons co-cultured with mouse microglia as indicated. Cell number ratio in co-cultures is 1:1. Neurons and microglia were both cultured from WT mice. **B**, Quantification of MAP2 staining positive area within the image field as readouts of surviving neurons in the culture. MAP2 areas are shown as normalized relative to the average value of control condition (no microglia, no stimulation). n = 4-5 per condition.

Fig. S5

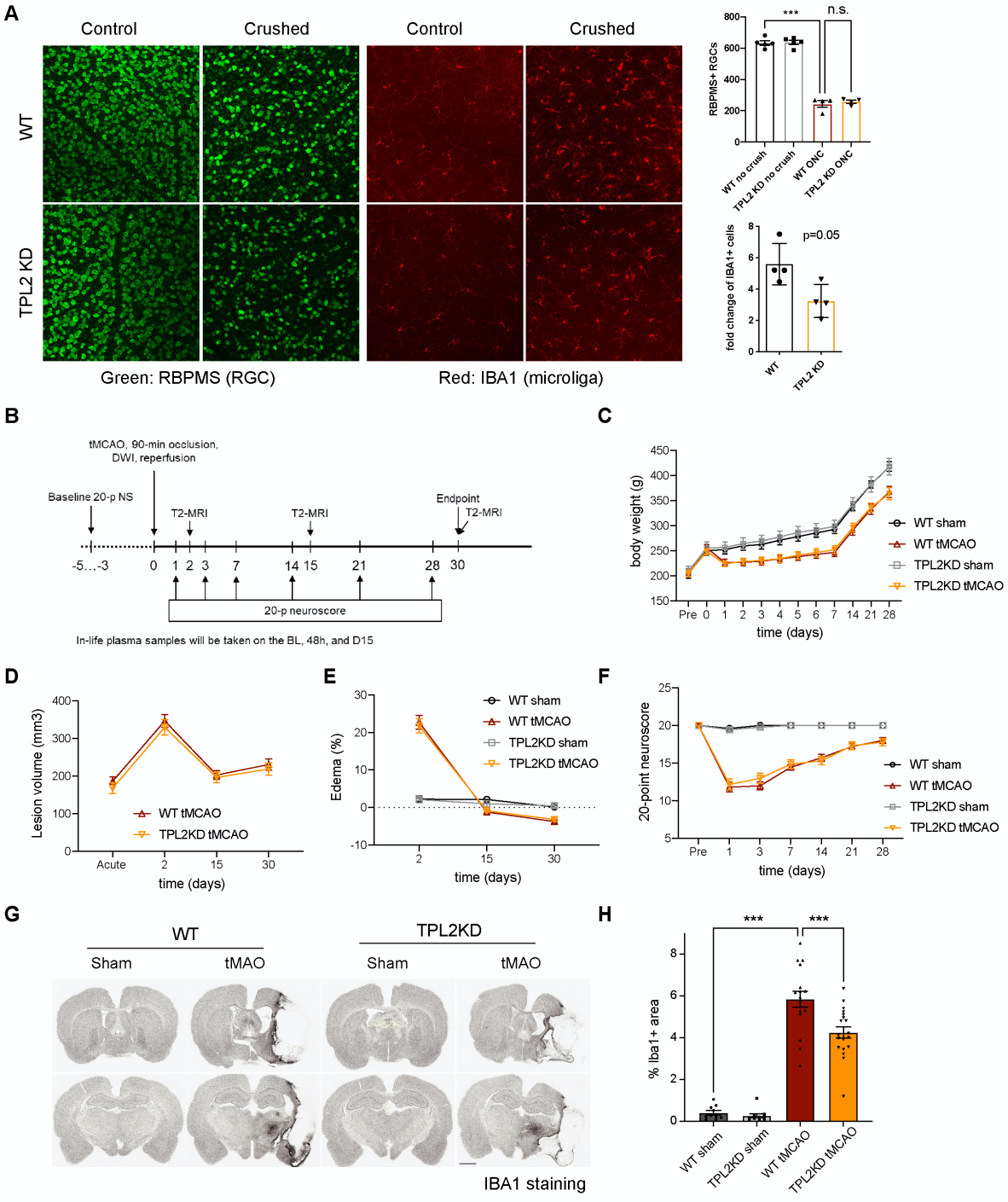

1285

1286

Fig. S5. Effect of TPL2KD in acute injury models: optic nerve crush and stroke.

A, *Left*, representative images of whole mount retina stained with RBPMS (green) for retinal ganglion cells (RGCs) and IBA1 (red) for microglia/macrophages from control eye or optic nerve crushed (ONC) eye of WT or TPL2KD mice as indicated. *Top Right*, quantification of the cell number of RGCs. *Bottom right*, quantification of the ratio of Iba1 positive cell number in the ONC eye relative the control eye of the same mouse. Each dot represents one mouse. Data are represented by mean +/- SEM. ***, $p < 0.001$, one-way ANOVA with Tukey's multiple comparisons test. **B**, Experimental design of rat tMAO study. **C**, Bodyweight measurements of WT and TPL2KD rats after sham or tMAO surgery at multiple timepoints as indicated. **D**, Quantification of lesion volume based on volumetric analysis of T2-relaxation time analysis from T2- MRI of WT or TPL2KD rats after tMAO surgery. **E**, Quantification of percentage of tissue area with Edema from T2-MRI of WT or TPL2KD rats after sham or tMAO surgery. **F**, Behavioral analysis of WT or TPL2KD rats after sham or tMAO surgery as indicated using 20-point neuroscore measurement. **G**, Representative images of Iba1 staining in WT and TPL2KD rats 30 days post-sham or -tMAO as indicated. Scale bar, 2 mm. **H**, Quantification of percentage of tissue area that are positive for Iba1 staining in the ipsilateral side of the rat brains. One mouse brain was excluded as outlier based on Grubb's test. Data are represented by mean +/- SEM. n = 10 for WT sham, n = 17 for WT tMAO, n = 9 for TPL2KD sham, n = 19 for TPL2KD tMAO. ***, $p < 0.001$, one-way ANOVA with Tukey's multiple comparisons test.

Fig. S6

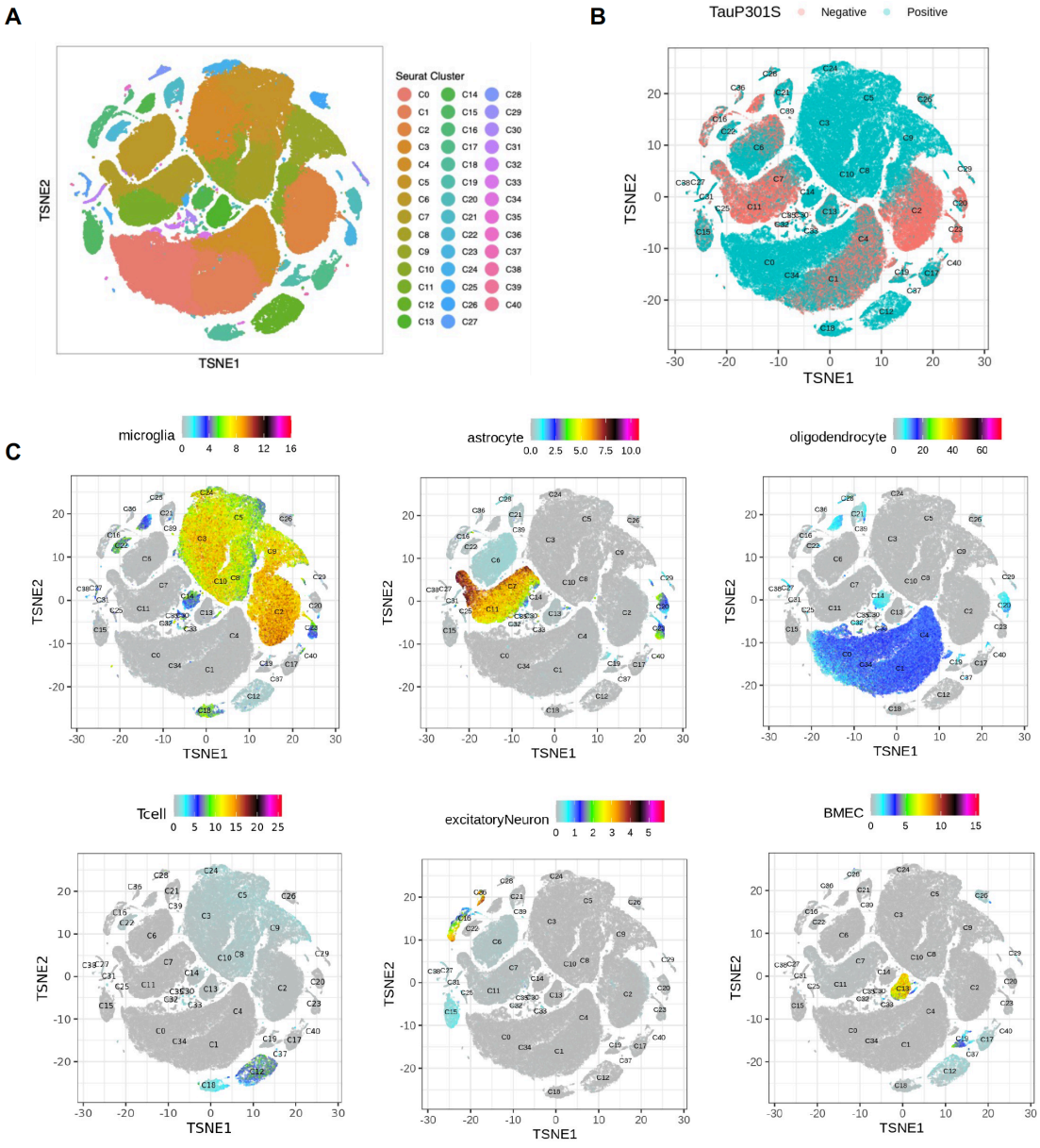

Fig. S6: Dimensional reduction and interpretation of cell clusters by gene set scores (related to Figure 5).

A, tSNE dimensional reduction and cell type interpretation of 142,752 hippocampal cells from 9-month-old TPL2 WT/KD TauP301S positive/negative mice. **B**, Distribution of cells by TauP301S phenotype. **C**, tSNE plots of gene sets marking specific cell type populations based on cell type specific markers from(Lee *et al.*, 2021b). Gene sets can be found in Table S1.

Fig. S7

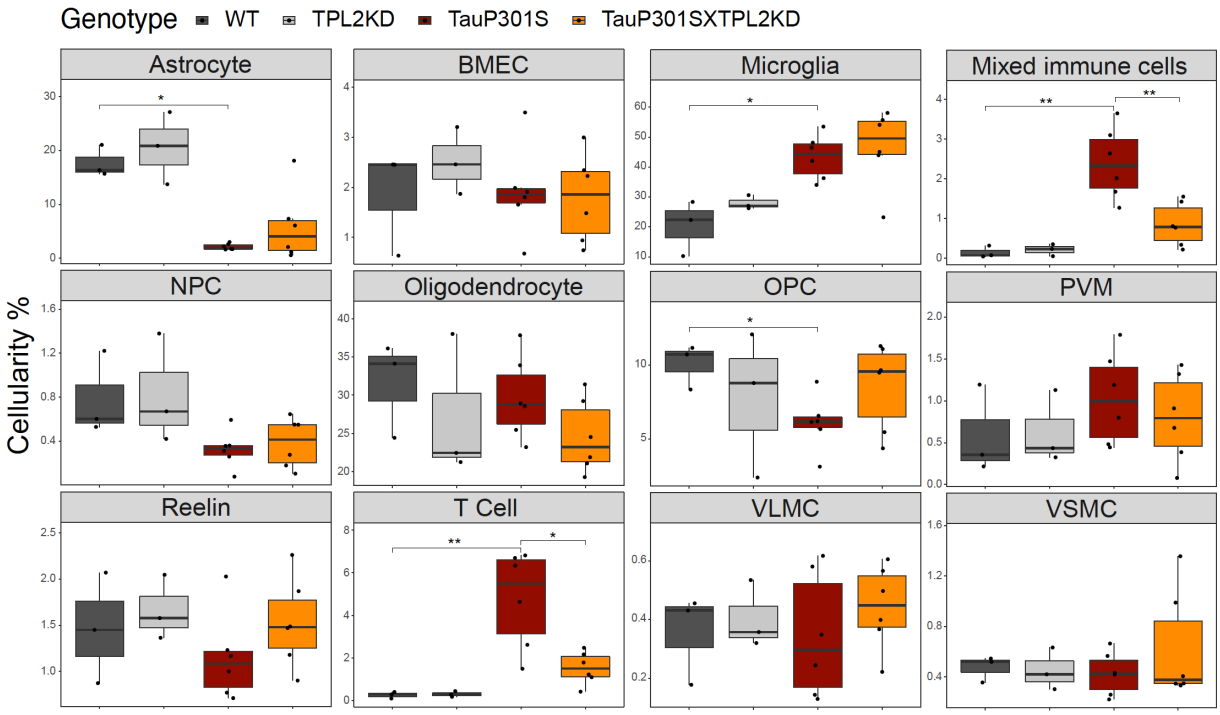

Fig. S7. Cellularity plot for all initially annotated cell types.

The percentage of cells in each cell type from Fig. 5A as percentage of the total number of cells wthin each sample (each dot is a sample). P values are based on t-test between indicated groups. *, $p < 0.05$, **, $p < 0.01$.

Fig. S8

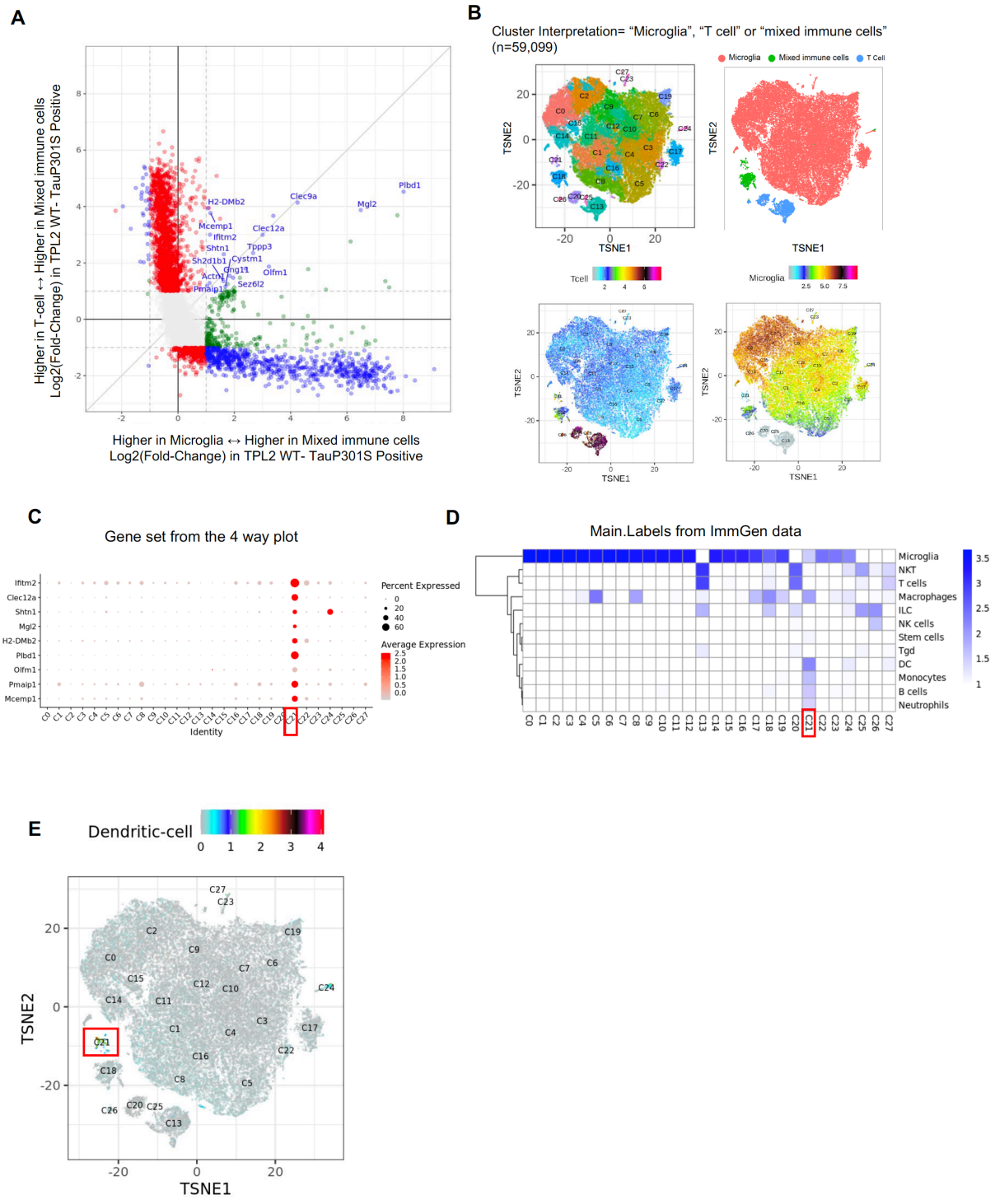

Fig. S8. related to Fig. 5. Identification of a unique cluster within the "mixed immune cell" cluster that corresponds to dendritic cells.

A, Scatter plot comparing gene expression fold-changes from T-cell vs. mixed immune cell cluster (x-axis) against fold-changes from Microglia vs. mixed immune cell clusters, as identified in Fig. 5A. Genes called as significantly differentially expressed (FDR < 0.05, Log2(fold-change) > 1 or < -1) are colored in red (T-cell vs. mixed immune cell), green (Microglia vs. mixed immune cell) or blue (both contrasts). X and Y axes represent gene expression on a log2 scale (log2(normCount+1)). Genes significantly enriched in mixed immune cell versus both microglia and T-cell populations are labeled, and these are potential candidate markers for a unique sub-population of the mixed immune cell that are distinct from microglia and T cells. **B**, tSNE dimensional reduction of immune cells (n = 59099; microglia n = 54523, T cell n = 2977 and mixed immune cells n = 1599), colored by sub-cluster, major cluster from Fig. 5A, or T-cell (Lee *et al.*, 2021b) or resting microglia (Friedman *et al.*, 2018) gene set scores (gene sets in Supplementary Table S1). Of note, C18 are microglia and T cell doublets. **C**, Dot plot showing the expression of potential candidate markers for the unique mixed immune subpopulation (as labelled in (**A**)) that are also identified as potential markers for immune cells sub-cluster C21 using FindMarkers function from Seurat package (Stuart *et al.*, 2019). **D**, Heatmap showing prediction scores for immune cells subclusters using SingleR and ImmGen dataset main labels (Heng *et al.*, 2008) from the celldex package (Aran et al., 2019). This analysis indicates the unique cell population in C21 most strongly corresponds to dendritic cells (DC). **E**, tSNE plot of genes marking C21 (dendritic) population using potential markers from (**A**).

Fig. S9

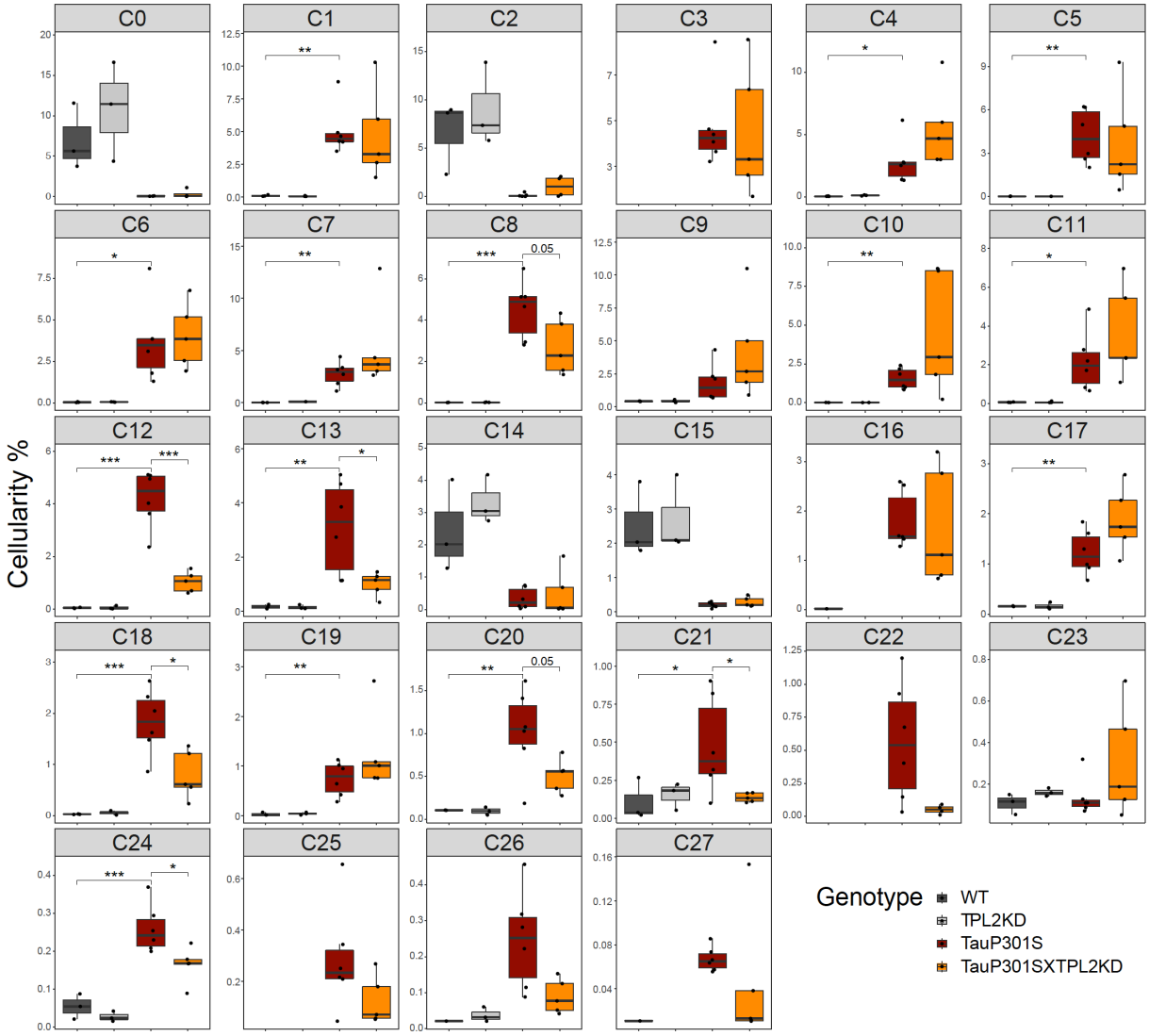

Fig. S9. Cellularity plot for all immune cell subclusters.

Proportions of immune cell subclusters (from Fig. S8B) as a percentage of total immune cells within each sample (each dot is a sample). P values are based on t-test between indicated groups. *, $p < 0.05$, **, $p < 0.01$, ***, $p < 0.001$.

1373 Fig. S10

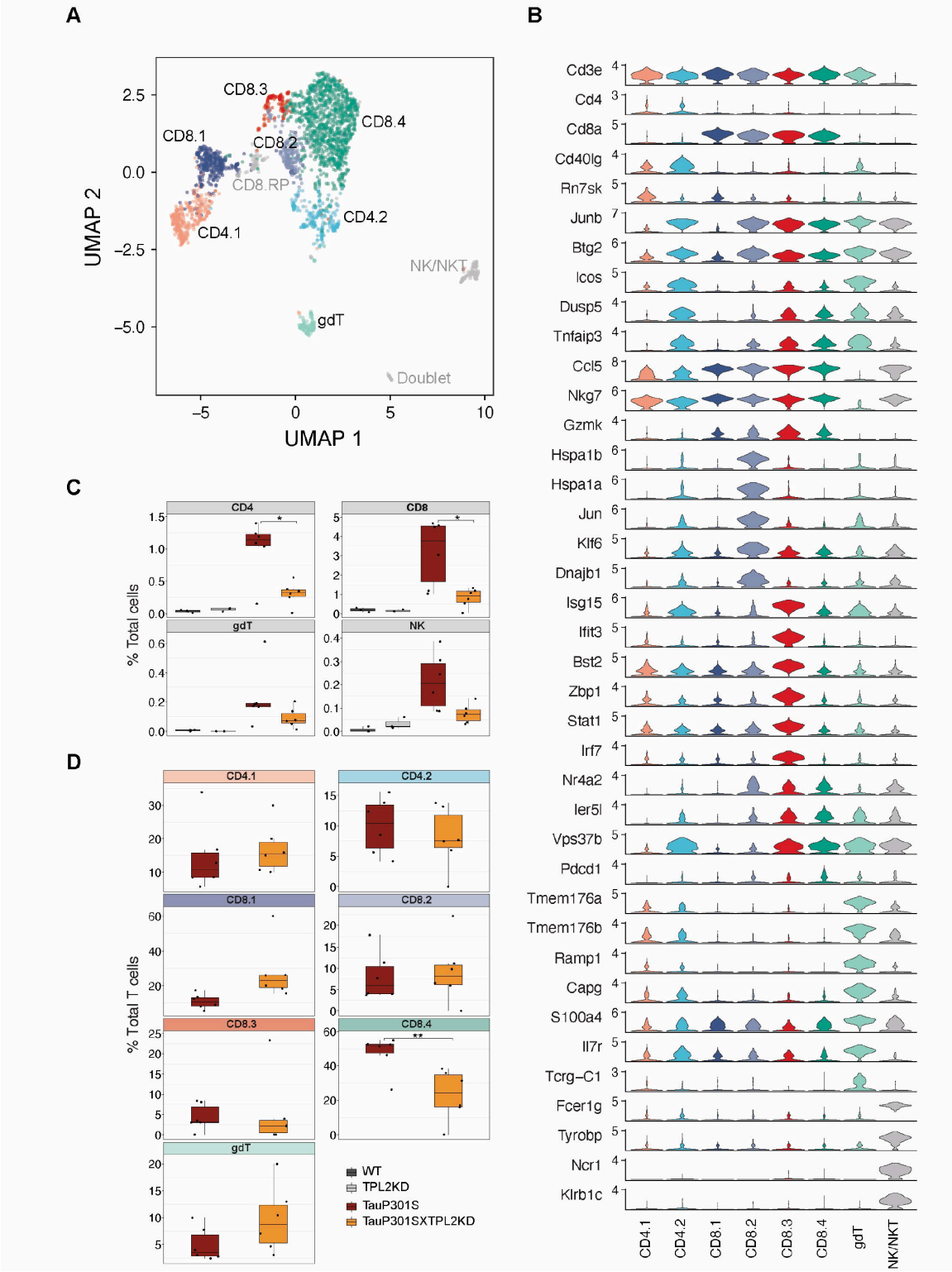

1374

1375

Fig. S10. Sub-clustering of T cells, related to Fig. 5.

A, UMAP dimensionality reduction and subclustering of 2,977 T cells defined from Figure 5A, colored by cell type interpretation. gdT = Gammadelta T cell, NK = Natural killer, RP = Ribosomal protein. **B**, Violin plots showing the log2 normalized expression of select genes representative for cell types identified in (**A**). (**C-D**) Cellularity plot, similar to Figure 5C, showing for each sample the percentage of T cell subtypes as a percentage of the total number of cells (**C**) or the total number of T cells (**D**) in that sample. P values are based on pairwise t-test with *Benjamini Hochberg* correction for multiple comparisons in (**c**) or t-test in (**D**). *, $p < 0.05$, **, $p < 0.01$.

1400 Fig. S11

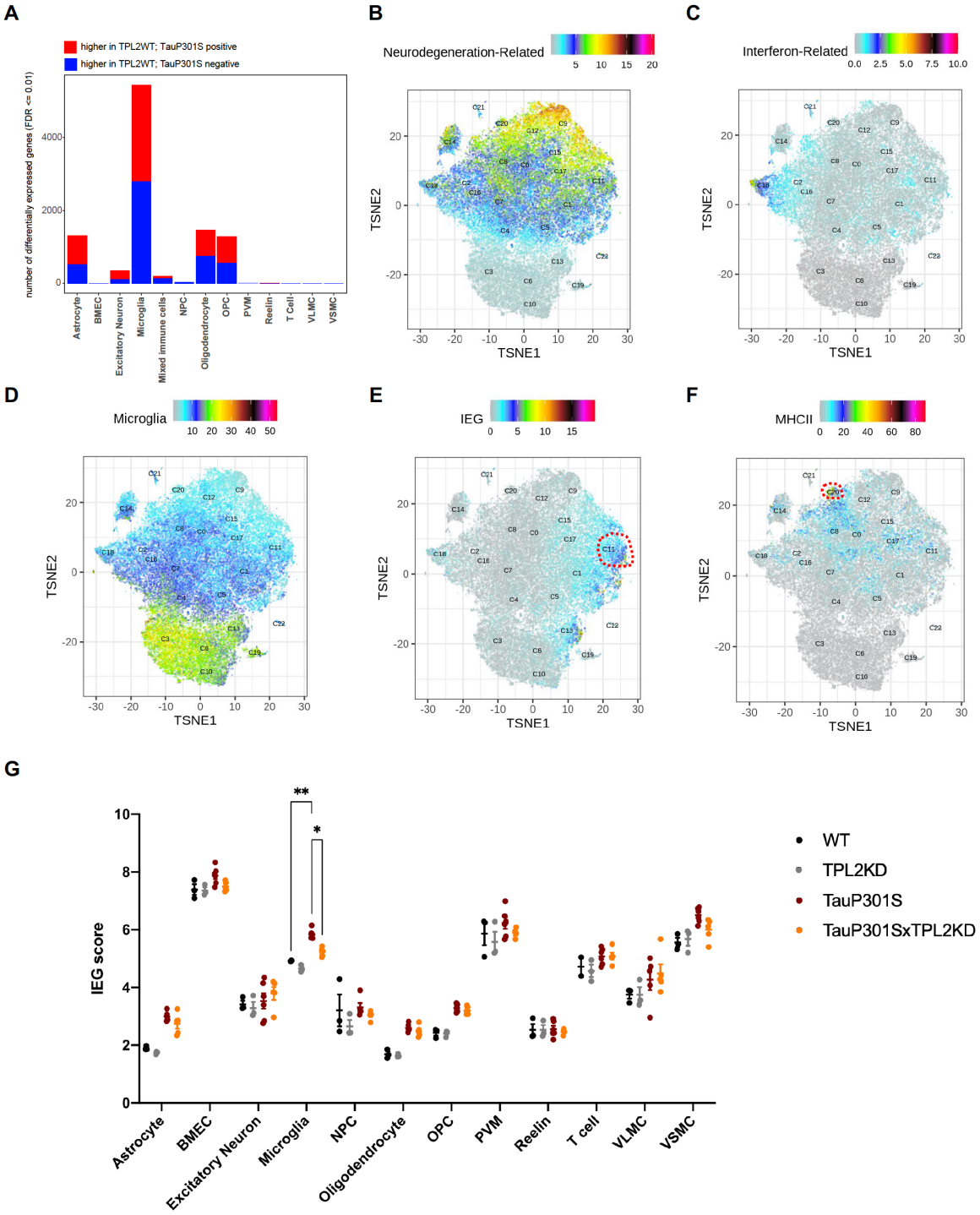

1401

1402

1403

Fig. S11. Related to Fig. 6. Sub-clustering of microglia and interpretation of cell activation states by gene set scores.

A, Number of significantly differentially expressed genes (DEGs) for each cell type from pseudobulk analysis at FDR < 0.01 and Log2(fold-change) > 1.5 or < -1.5 between TauP301S positive and non-transgenic samples (TauP301S negative) across cell types from Fig. 5A. **B-F**, tSNE dimensional reduction of microglia cells (n = 54,523) colored by average/combinatorial expression of genes belonging to the indicated sets (DAM, IFN, Resting MG, IEG and MHCII). All gene sets used in this study are provided in Table_S1. **G**, Strip plot showing expression levels of IEG gene sets in each of the 4 genotypes in this study across all cell types from Fig. 5A. Data are represented by mean +/- SEM. *, $p < 0.05$, **, $p < 0.01$, ***, $p < 0.001$, Two-way ANOVA with Tukey's multiple comparisons test.

1428 Fig. S12

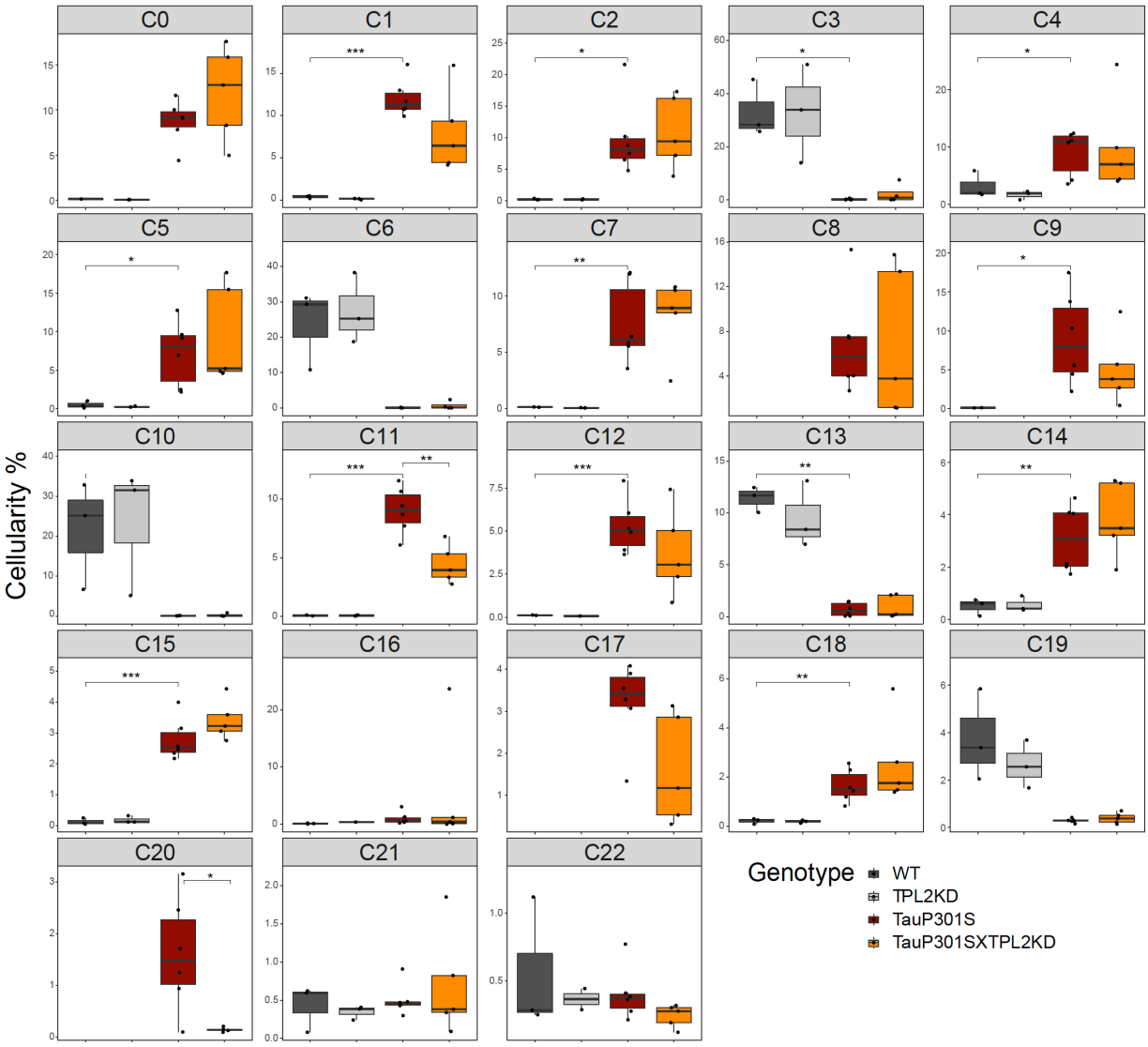

1429

1430

1431 **Fig. S12. Cellularity plot for microglia cells.**

1432 similar to Fig. 5C, illustrating proportions of each microglia subcluster as a percentage of total

1433 microglia cells within each sample (each dot is a sample). P values are based on t-test between

1434 indicated groups. *, $p < 0.05$, **, $p < 0.01$, ***, $p < 0.001$.

1435